

Assessment of Existing Steel Frames: Numerical Study, Pseudo-Dynamic Testing and Influence of Masonry Infills

Luigi Di Sarno^{1*}, Fabio Freddi², Mario D’Aniello³, Oh-Sung Kwon⁴, Jing-Ren Wu¹, Fernando Gutiérrez-Urzúa², Raffaele Landolfo³, Jamin Park⁴, Xenofon Palios⁵ and Elias Strepelias⁵

¹*Dept. of Civil Eng. & Industrial Design, University of Liverpool, L69 3GH, Liverpool, U.K.*

²*Dept. of Civil, Environmental & Geomatic Engineering, University College London, London WC1E 6BT, U.K.*

³*Dept. of Structures for Eng. & Architecture, University of Naples Federico II, 80134 Naples, Italy*

⁴*Dept. of Civil and Mineral Eng., University of Toronto, M5S 1A4, Toronto, Canada*

⁵*Structures Laboratory (STRULAB), Civil Eng. Dept., University of Patras, 265 04, Patras, Greece*

*Corresponding Author. E-mail address: luigi.di-sarno@liverpool.ac.uk

ABSTRACT

Most of existing steel multi-storey frames in Europe have been designed before the introduction of modern seismic design provisions, hence they often exhibit low performance under earthquake loads due to their low lateral resistance and energy dissipation capacity. In addition, such structures often include rigid and brittle masonry infill walls that highly influence their lateral response and distribution of damage pattern. However, current procedures for the assessment of existing steel buildings in Europe, included in the Eurocode 8 – Part 3 (EC8-3), do not provide adequate guidance for the assessment of ‘weak’ steel frame with masonry infill walls. Moreover, most of available modelling approaches of masonry infills formerly developed for reinforced concrete (RC) structures do not properly represent the behaviour of infill walls in steel frames. An improved numerical has to be provided to satisfactorily mimic infill walls’ behaviour in steel moment frames. To this end, an experimental and theoretical study was carried out within the framework of HITFRAMES (*i.e.*, Hybrid Testing of an Existing Steel Frame with Infills under Multiple Earthquakes) SERA project. This paper firstly presents the limitations of current EC8-3 by conducting a code-based assessment on a case study steel moment frame using pushover analysis. Three different single strut models, widely used for simulating the presence of masonry infills in RC structures, are considered for the numerical analyses. The paper also presents the results of pseudo-dynamic (PsD) tests performed on a large-scale 3D steel frame with masonry infills. The capability of the different masonry infill models is successively evaluated by comparisons between numerical and experimental results. On the basis of the obtained results, recommendations on how to potentially improve the single strut model for masonry infills surrounded by steel frames are also provided.

Keywords: Existing steel frames; Seismic performance; Pseudo-Dynamic Testing; Masonry infills; Single-strut model.

1 INTRODUCTION

Many existing steel structures worldwide were built before the introduction of modern seismic design provisions and hence may exhibit high seismic vulnerability due to lack of seismic resisting system, proper seismic detailing, and inadequate energy dissipation capacity [1]. A recent post-earthquake study [2] highlighted several failure patterns on an existing steel moment-resisting frame (MRF), which is located in the area hit by the 2016 Central Italy earthquakes. It was reported that steel MRFs suffered large residual lateral drifts with significant yielding at beam-column connections and soft storey mechanism. Severe damage was also found on non-structural components, including in-plane and out-of-plane failure of masonry infill walls and partial collapse of finishing plasters. Figure 1 presents some examples of typical damage observed on existing steel frames. Similar failure pattern on steel MRFs was also observed in many other post-quake studies, including the 2010-2011 Christchurch earthquakes in New Zealand [3], the 1994 Northridge earthquakes in the US [4, 5], 2011 Tohoku-Oki earthquakes in Japan [6], 2010 Maule Earthquake in Chile [7, 8], etc. In this context, there is a significant need to develop an advanced assessment framework, which can properly quantify the seismic vulnerability of existing steel buildings, especially accounting for the contribution from non-structural components, and able to support retrofit strategies.

The assessment framework available in the current EN1998-3 (hereinafter referred to as EC8-3) [9] is considered outdated [Error! Reference source not found.]. Among others, one of the main drawbacks of the current version of the EC8-3 is the lack of consideration for the effects of masonry infills, which have demonstrated to significantly affect the seismic behaviour of existing steel frames in many occasions. Previous studies have shown that the effects of masonry infill on the seismic performance of frame structures are evident [*e.g.*, 11, 12, 13, 14, 15, 16]. On the one hand, the presence of masonry infill can increase the lateral stiffness and strength of bare frames, as well as the energy dissipation capacity under seismic loadings. On the other hand, strut action of infill walls can also lead to increased local seismic demands, particularly at beam-to-column connections. As a result, several modelling strategies of masonry infill have been developed in literature in order to adequately consider the masonry infill contribution in the seismic assessment of existing buildings (*e.g.*, the models by Decanini and Fantin [17]; Fardis and Panagiotakos [11]; Dolšek and Fajfar [12]; Crisafulli

62 and Carr [18]; Liberatore and Decanini [19]; Uva et al. [20]; Mohammad Noh et al. [21]; Liberatore et al. [22]). Most of
63 the popular modelling approaches utilise a single strut solely active in compression in each diagonal direction of the infill
64 wall panel, hence the name single-strut model. Such models have been proved to be capable of predicting the global
65 response of structures at a low computational cost. However, almost all single-strut models available in the literature were
66 developed for, or calibrated based on infills walls within reinforced concrete (RC) frames. Since steel frames tend to be
67 more flexible and more ductile than RC frames, and steel members tend to show different local details, *e.g.*, interactions
68 between column flanges and infill walls, it is unclear to what extent these models can be used to represent masonry struts
69 in steel frames. To this end, there is a need for advanced studies investigating the behaviour of masonry infill within steel
70 frames, thus allowing the development of adequate numerical models to be used in seismic assessment procedures.
71



Figure 1. Typical damage on existing steel MRFs: (a) yielding of structural components; (b) fracture (ultimate failure) of structural components (from Ricles *et al.*, 2011 [35]); (c) cracking of masonry infills; (d) collapse (out-of-plane failure) of masonry infills.

72
73 Another essential aspect that needs to be addressed in the next generation of EC8-3 is the impact of earthquake sequences.
74 In most natural seismic events, mainshocks are often accompanied by several foreshocks and aftershocks with comparable
75 magnitudes during seismic events, which can lead to large cumulative seismic demand on existing structures [23, 24, 25].
76 Premature fracture and local buckling may occur in plastic hinges, especially of steel columns (see Figure 1(a) and (b),
77 respectively), thus leading to stiffness reduction and strength deterioration. The seismic response of masonry infill with
78 steel buildings is also greatly affected by the earthquake sequences, as observed in the recent Central Italy earthquake
79 (see Figure 1(c) and (d)). Extensive inelastic analyses have been recently carried out to investigate earthquake sequence
80 effects on inelastic displacement demands of steel buildings [26, 27, 28, 29]. Some studies have focused on the response
81 of infilled RC frames subjected to mainshock-aftershock sequences [30, 31, 32, 33, 34]; however, research on the
82 performance of infilled steel frames subjected to earthquake sequences is still limited.
83

84 The present paper aims to investigate the impact of masonry infill on the seismic performance of existing steel MRFs,
85 taking into consideration the influence of earthquake sequences. The selected case study building is a two-storey steel
86 MRF designed primarily for gravity loads with insufficient seismic detailing. Hence, it was considered representative of
87 non-seismically designed steel frames based on the characteristics observed in the steel frame in Amatrice [2, 16]. The
88 performance of the steel building, as part of the HITFRAMES SERA Project, was experimentally investigated through
89 pseudo-dynamic (PsD) tests at the Structures Laboratory (STRULAB) of the University of Patras, Greece, which is among
90 the few European laboratories employing the PsD testing method with sub-structuring hybrid simulations.

Numerical modelling of cyclic behaviour of infill walls is still very challenging. To accurately evaluate the seismic response of a steel frame with infill walls, PsD test was adopted in this study. In PsD test, the mass and damping properties of a structure are modelled numerically, while the restoring force from the infill walls and steel frame is obtained experimentally. In the adopted PsD test, the numerical integration scheme predicts the displacements imposed by the actuators to the lab specimen [36, 37, 38] and hence, it allows simulating the dynamic response of a structure by imposing the displacements in a quasi-static manner. This testing procedure requires ‘conventional’ laboratory facilities (e.g., the actuators and reaction walls), and hence it is often preferred to the more complex and expensive shake table tests. Despite the advantages of PsD tests, this method cannot accurately model rate-dependent behaviour of structural elements, such as viscous dampers, compared to the shake table test or the more recently developed real-time PsD test [39, 40]. In typical steel, concrete, or masonry structures, the cyclic response of the structural elements does not depend on the rate of loading imposed by earthquake events [41], and the stress relaxation due to slow loading-rate is negligible [42].

Two configurations of the case study building are considered in the study, the prototype and the tested mockup. The two-storey prototype building is comprised of three bays and one bay in the longitudinal and transverse directions, respectively. On the other hand, the tested frame is a scaled one-bay sub-structure of the central bay of the prototype building in the longitudinal direction. In the first part of the paper, the influence of masonry infill walls on the seismic performance of the prototype building is investigated through pushover analysis performed according to the EC8-3 [9]. A non-linear finite element (FE) model of the case study building is developed in OpenSees [36], where masonry infills are modelled using diagonal struts calibrated according to the ‘real’ properties of the materials that were used to build the lab specimen. In the second part of the paper, the PsD tests of the infilled steel frame are presented together with experimental results, including a description of the damage scenario and the cyclic response recorded at each storey. In parallel, a numerical model is also built for the tested frame and is subjected to the same storey displacements history recorded during the PsD tests. The response of the numerical model is then compared to the experimental results, allowing the identification of the limitations and drawbacks of the current modelling strategies for masonry infills in steel frames, also providing insights for future research on the definition of more adequate and reliable models.

2 EUROPEAN CODES FOR SEISMIC ASSESSMENT OF EXISTING BUILDINGS

This section of the paper provides the essential background information of standardised procedure for the seismic assessment of existing steel MRFs based on the EC8-3. The discussion is further enhanced by the critical comparisons with some of the recommendations of EN1998-1 (EC8-1) [44]. Among others, it is noteworthy that while EC8-1 covers all aspects related to the seismic design, the EC8-3 covers the seismic assessment and retrofit of existing structures. Hence, although these two codes have a common background, their aims are different, thus resulting in some substantial differences that affect both structural analysis and verification.

The EC8-3 [9] defines three limit states for the seismic assessment of existing buildings, namely Damage Limitation (DL), Significant Damage (SD) and Near Collapse (NC) limit states. On the contrary, EC8-1 considers two limit states only, namely Damage Limitation (DLS) and Ultimate (ULS) limit states. Each limit state is checked at different levels of seismic hazard, as summarised in Table 1. As it can be observed, the return period considered for the damage limitation objectives is different between the EC8-3 and EC8-1. This aspect is not contradictory because it depends on the different objectives of the codes. For the sake of clarity, the EC8-1 considers more frequent earthquake at the DLS in order to limit the reparation costs of the non-structural components in newly designed structures. Conversely, the EC8-3 considers a rarer seismic event to limit the structural damage for ease of reparability, thus accepting the collapse of non-structural elements. ULS and SD limit states have almost the same objectives. Therefore, the same return period is considered in both codes. A substantial difference between the two codes is related to the NC limit state that is not defined in EC8-1. The reason of such difference is related to the fact that EC8-1 is a design code, which prescribes design and detailing rules that guarantee adequate sources of ductility and overstrength to cover the demand at NC. Therefore, the code is calibrated to implicitly satisfy the performance at NC because the designer has to comply with specific measures that are properly (or supposed to be) calibrated by the code drafter. On the contrary, EC8-3 deals with existing structures that are not code-compliant. Therefore, it explicitly needs to verify their performance even at NC.

Table 1. Return period and associated probability of exceedance of limited states in EC8-3 [9] and EC8-1 [44].

Limit States	EC8-3			EC8-1	
	DL	SD	NC	DLS	ULS
Return Period	225 yrs.	475 yrs.	2475 yrs.	95 yrs.	475 yrs.
P _{exceedance}	20% in 50 yrs.	10% in 50 yrs.	2% in 50 yrs.	10% in 10 yrs.	10% in 50 yrs.

The first key step of the assessment procedure is the definition of the knowledge level (KL). The EC8-3 defines three KLS to account for the potential lack of information of existing buildings, such as the geometry and material properties.

148 Each knowledge level is associated with the allowed methods of analysis for the seismic assessment. Linear analysis
 149 methods are allowed for all three KLS, while non-linear approaches are only allowed for ‘normal knowledge’ (KL2) and
 150 ‘full knowledge’ (KL3). Besides, each knowledge level is associated with a confidence factor (CF) that should be used to
 151 reduce the mean value of material strength. The CFs are 1.35, 1.20 and 1.00 for KL1 (*i.e.*, ‘limited knowledge’), KL2 and
 152 KL3, respectively. After determining the knowledge level, the numerical model of the structure can be established with
 153 the modified material properties.

154
 155 The following step is the definition of the seismic demands. Both the non-linear static (pushover) and non-linear dynamic
 156 (time-history) analysis approaches are allowed in EC8-3 for KL2 and KL3; however, pushover analysis is usually easier
 157 to be performed while time-history analysis can be cumbersome and time-consuming for complex structures. For this
 158 reason, the pushover analysis procedure has become the most widely used analysis method within the context of the
 159 seismic assessment of existing structures. The EC8-3 requires two lateral load patterns, namely ‘uniform’ and ‘modal’
 160 pattern, to be applied in pushover analysis. After obtaining the pushover curves, the seismic demands are then determined
 161 according to the N2 method [46], which transfers the structures into an equivalent SDOF system based on the first mode
 162 shape and uses the target response spectrum in acceleration-displacement form.

163
 164 On the other hand, the implementation of time-history analysis is more complex compared to the pushover analysis, as it
 165 requires accurate definition of non-linear hysteretic behaviour of components calibrated against experimental results. The
 166 EC8-3 requires at least three ground motion records to be used, whose mean response spectrum achieves compatibility
 167 with the target spectrum, *i.e.*, the mean spectrum should not be less than 90% of the target spectrum within the range
 168 $[0.2T_1, 2T_1]$, where T_1 is the fundamental period of the structure. Besides, the EC8-3 also requires that the two horizontal
 169 ground motions should be applied simultaneously to the assessed structure when a spatial model is used in the analysis.

170
 171 The final stage of the assessment procedure consists in the safety verification. For ductile components of steel MRFs, the
 172 EC8-3 compares the rotation demands at the end of beams and columns with their corresponding rotational capacity limits.
 173 Capacity limits are defined as inelastic chord rotation thresholds determined as a multiple of the chord rotation at yielding
 174 θ_y . under the condition that the dimensionless axial load v of a member is not larger than 0.3, as summarised in Table 2.
 175 However, it is noteworthy that the EC8-3 does not provide any guidance on the determination of yield rotation at the end
 176 of steel beams and columns, or any criteria for the cases with axial force higher than 0.3 times the plastic axial resistance
 177 of the member (*i.e.*, $v > 0.3$). An extensive discussion on the capacity limits for beams, columns and panel zones is
 178 provided in Gutiérrez-Urzúa *et al.* 2021 [Error! Reference source not found.].

179
 180 Table 2. Plastic rotation capacity at the end of beams and columns in EC8-3.
 181

Class of cross-section in accordance with EN1993-1	Limit state		
	DL	SD	NC
Class 1	1.0 θ_y	6.0 θ_y	8.0 θ_y
Class 2	0.25 θ_y	2.0 θ_y	3.0 θ_y

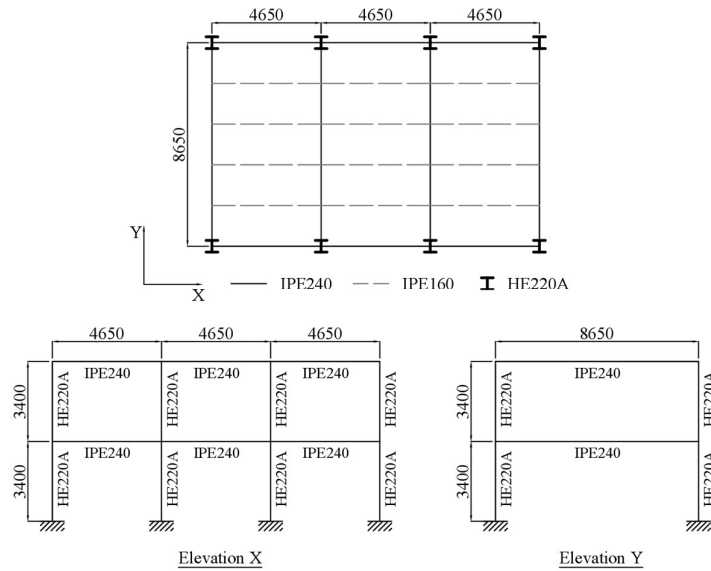
182
 183 Moreover, it should be noted that the current version of EC8-3 does not provide specific requirements to account for the
 184 effects of masonry infill, although the performance of non-structural components is included in the definition of limit
 185 states. Besides, the EC8-3 does not give any criteria to model and verify the non-linear behaviour of infill panels and their
 186 interaction with the primary structure for pushover analysis as well as no relevant criteria are provided to evaluate the
 187 performance of the masonry infills at different limit states. Therefore, in the light of all these considerations, the rules and
 188 requirements given by the current version of EC8-3 do not suffice to allow performing a comprehensive and effective
 189 assessment of existing steel MRFs with masonry infills.

191 3 DESCRIPTION OF THE PROTOTYPE BUILDING AND THE TEST FRAME

192 3.1 The prototype building

193
 194 A benchmark two-storey, three-bays by one-bay MRF was designed as the prototype building, which is a representative
 195 of non-seismically designed, low-ductility, low-rise steel building. The building was designed for gravity loads only
 196 following the European design guidance for steel buildings, Eurocode 3 (EC3) [47], and without sufficient seismic
 197 detailing. Furthermore, as per the EC3, wind loads are considered negligible for low-rise structures, such as the case study
 198 steel frame, leading to a complete lack of lateral loading resisting system in the frame design. The gravity design was
 199 conducted considering a non-structural permanent load, *i.e.*, walls and other finishing including internal partitions, equal
 200 to 2.58 kN/m² while the considered use category was ‘offices area’ and hence the characteristic value of the imposed load
 201 was assumed equal to 3 kN/m².
 202
 203

204 The prototype building is characterised by storey height of 3.4 m, with slight variations between the two stories. The span
 205 is 8.65 m and 4.65 m along the longitudinal and transverse direction, respectively. An overview of the structural system
 206 both in plan and in elevation, including the main geometric parameters and section members, is reported in Figure 2. The
 207 steel profiles are HE 220 A, IPE 240 and IPE 160, respectively, for columns, primary and secondary beams. The steel
 208 grade is S355 ($f_y = 355$ MPa) for all beams and columns. All external beams are connected to columns through full
 209 penetration welds, and fully rigid beam-column connections are considered in this study. The floor system was designed
 210 as a composite slab, with a cold-rolled steel sheet base ($t = 1.25$ mm) and a 200-mm-deep concrete slab with M19 shear
 211 studs at each valley or 300 mm, depending on the steel sheet rib orientation. Lastly, the masonry infills consist of two
 212 parallel layers of perforated bricks separated by insulation materials, each of which has a thickness of 58 mm. According
 213 to the final design and considering the EC8-1 [41] seismic combination, the building's storey mass is equal to 117.0 and
 214 95.0 tons, respectively, for the first and second storey. In order to investigate the performance of the structure in its weaker
 215 and more deformable direction, the steel frame was tested under a horizontal load in the x -direction, as indicated in Figure
 216 2, where the columns are oriented with their weak axis.
 217



218
 219 Figure 2. Global geometry of the prototype building: plan view and elevations (unit: mm).
 220

221 For the assessment, conducted according to the EC8-3 [9], the full knowledge of the structure, *i.e.*, knowledge level 3
 222 (KL3), corresponding to a confidence factor (CF_{KL3}) equal to 1.0, was assumed. In order to comply with the requirements
 223 established by the EC8-3 [9] to reach the KL3, the material properties were determined based on coupon tests sampled
 224 from all steel components, as well as compression and diagonal compression tests of masonry samples. This allowed the
 225 prototype building assessment by referring to actual material properties for structural steel and for masonry infills, as
 226 described in the next section.
 227

228 3.2 The test mockup – scaling and similitude of the prototype building

229
 230 The test mockup consisted in the central-bay sub-structure of the 75% scaled (*i.e.*, scaling factor $\lambda = 0.75$) model of the
 231 prototype building, *i.e.*, the two-storey, three-bays by one-bay steel MRF. The model scaling is based on the material and
 232 acceleration scaling identity [48], and the scaling factor was selected considering the laboratory constraints and
 233 accounting for that usually a scaling factor larger than 0.6 is adequate to allow the test to correctly reproduce the seismic
 234 response of steel frames. The use of unit scale factor for material stress is a common and convenient choice, as it allows
 235 to overcome difficulties in the replication of every mechanical property of the prototype building (*e.g.*, Poisson ratio,
 236 failure strain, etc.). Table 3 reports the list of the scaling factors of similitude between prototype building and test frame.
 237 However, it should be noted that the scaling factor was not applied to the thickness of infill walls due to limited availability
 238 of smaller perforated bricks in the local market. Despite that, the infill walls with unscaled thickness could still fit the
 239 space in between the flanges of columns and behave as two separate brick layers with high slenderness, hence were of
 240 the same features as the infill walls in the prototype building. Moreover, considering that the scaling factor adopted ($\lambda =$
 241 0.75) was close to the unit and considering the variability of thickness for masonry infills, the unscaled thickness of infill
 242 walls would not significantly increase the strength of the test mockup, hence could be still considered representative of a
 243 real case study.
 244

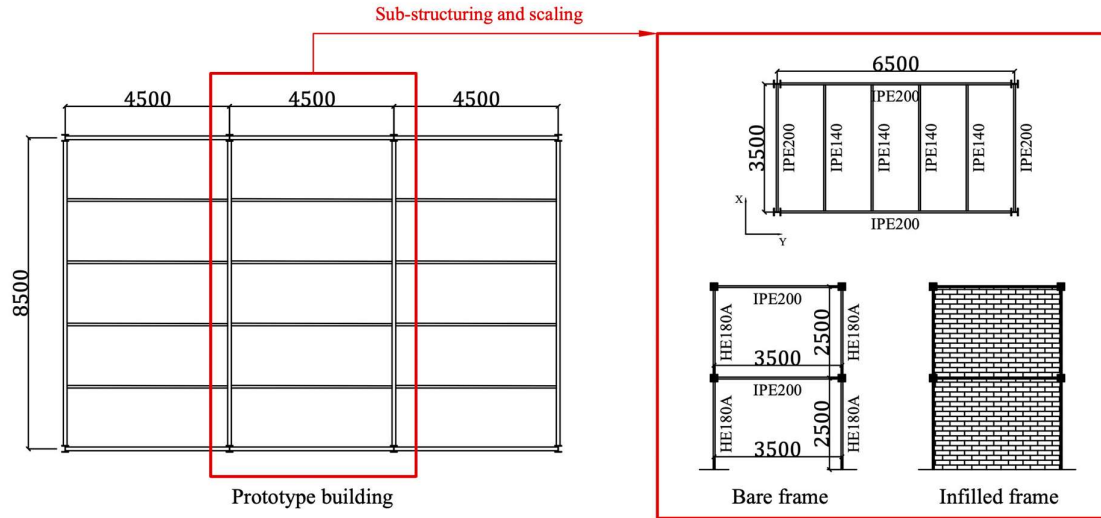


Figure 3. Plan and side views of the test specimens (unit: mm).

245



Figure 4. Positions of stiffeners at (a): beam-column connections and (b) column bases.

246

247

248

Table 3. Similitude scaling factors with $\lambda = 0.75$.

Parameter	Scaling factor
Density	$\lambda^{-1} = 1.33$
Stress, strain, angular deformation and acceleration	$\lambda^0 = 1$
Period, time and velocity	$\lambda^{1/2} = 0.87$
Length, linear deformation and stiffness	$\lambda^1 = 0.75$
Force, weight, mass and area	$\lambda^2 = 0.56$
Volume, section moduli and moment	$\lambda^3 = 0.42$
Moment of inertia	$\lambda^4 = 0.32$

249

250

251

252

253

254

255

256

257

258

259

260

261

The procedure of scaling and sub-structuring of the prototype building is illustrated in Figure 3. The test mockup has a storey height of 2.5 m and span of 3.5 m in the transverse direction and of 6.5 m in the longitudinal direction. The steel profiles of the test frame are summarised in Table 4. Profiles HE 180A, IPE 200 and IPE 140 were respectively used for columns, primary and secondary beams. All external beams were connected to columns through full penetration welds, and stiffeners were used to increase the connection rigidity, as shown in Figure 4. In addition, the composite slab of the test specimen consisted of 150 mm-thick concrete slab poured on 1.25 mm-thick corrugated steel sheet. M19 shear studs were used at each valley or with a 300 mm spacing, depending on the steel sheet ribs orientation. The distribution of shear studs ensured the transfer of actuator-applied horizontal loading with the exception of 0.5-m-wide regions around each joint where studs were omitted. This type of detail is commonly used to avoid the development of composite actions in the joints. Lastly, masonry infills considered for the test frame consisted of double-leaf, 58 mm-thick each, perforated bricks made up of 58 mm \times 83 mm \times 190 mm units (the insulation materials were omitted). The final storey mass of the test mockup was equal to 23.5 and 20.0 ton for the first and second storey, respectively.

262
263
264

Table 4. Geometric properties of the case study frame before and after scaling.

	Unit	Prototype building	Lab specimen
Storey height	(m)	3.4	2.5
Bay width	(m)	4.65	3.5
Span	(m)	8.65	6.5
Column	(-)	HE 220A	HE 180A
Main beam	(-)	IPE 240	IPE 200
Secondary beam	(-)	IPE 160	IPE 140

265
266
267
268
269
270
271
272
273
274
275
276
277
278
279
280

3.3 Material properties for structural steel and masonry infills

Material tests were conducted to implement numerical models of the case study steel frame; such tests included coupon tests for steel, compression and shear tests for masonry infill. To fulfil the requirement of KL3 as per EC8-3 [9], the steel coupons were obtained directly from the test frame while the masonry units were built using the same technique as the masonry infill walls in the test frame.

Coupon tests for steel

Coupons cut from both web and flanges of beams and columns of the test frame were tested according to the BS EN ISO 6892-1 [49]. The upper yield and the peak stress points of the stress-strain curve were taken as yield and ultimate strength. The results are summarised in Table 5 to Table 7.

Table 5. Yield and ultimate stress (μ : mean value; σ : standard deviation; CoV: coefficient of variation).

Profile		Quantity	Yield stress			Ultimate stress		
			μ (MPa)	σ (MPa)	CoV (%)	μ (MPa)	σ (MPa)	CoV (%)
Beam (IPE200)	Flange	8	408.94	17.22	4.21	561.92	17.70	3.15
	Web	4	426.38	11.43	2.68	558.47	9.61	1.72
Column (HE180A)	Flange	8	424.06	8.99	2.12	592.21	9.27	1.57
	Web	4	450.32	12.53	2.78	583.42	7.94	1.36

281
282
283

Table 6. Yield and ultimate strain (μ : mean value; σ : standard deviation; CoV: coefficient of variation).

Profile		Quantity	Strain at yielding			Strain at ultimate stress		
			μ (-)	σ (-)	CoV (%)	μ (-)	σ (-)	CoV (%)
Beam (IPE200)	Flange	8	0.0023	0.0005	21.74	0.1370	0.0038	2.77
	Web	4	0.0020	0.0002	10.00	0.1306	0.0067	5.13
Column (HE180A)	Flange	8	0.0031	0.0007	22.58	0.1355	0.0076	5.61
	Web	4	0.0026	0.0003	11.54	0.1419	0.0067	4.72

284
285
286

Table 7. Overstrength and ductility (μ : mean value; σ : standard deviation; CoV: coefficient of variation).

Profile		Quantity	Overstrength			Ductility at ultimate stress		
			μ (-)	σ (-)	CoV (%)	μ (-)	σ (-)	CoV (%)
Beam (IPE200)	Flange	8	1.13	0.02	1.77	61.77	15.61	25.27
	Web	4	1.31	0.02	1.53	64.59	4.50	6.97
Column (HE180A)	Flange	8	1.40	0.02	1.43	45.73	11.89	26.00
	Web	4	1.30	0.03	2.31	54.79	7.93	14.14

287
288
289
290
291

The mean values of yield stress of all tested steel components were higher than the characteristic strength of S355 steel. The yield stresses of column flanges and webs were 424.06 and 450.32 MPa, respectively, which are approximately 4-5% higher than the yield stress of beam flanges and webs.

292 *Compression test on the infill panels*

293

294 Material properties for masonry infills were investigated through masonry compression tests according to the EN 1052-1
 295 [50] recommended by Eurocode 6-Part 1-1 [51]. The typical test setup is shown in Figure 5(a), while the stress-strain
 296 curves are reported in Figure 5(b).
 297

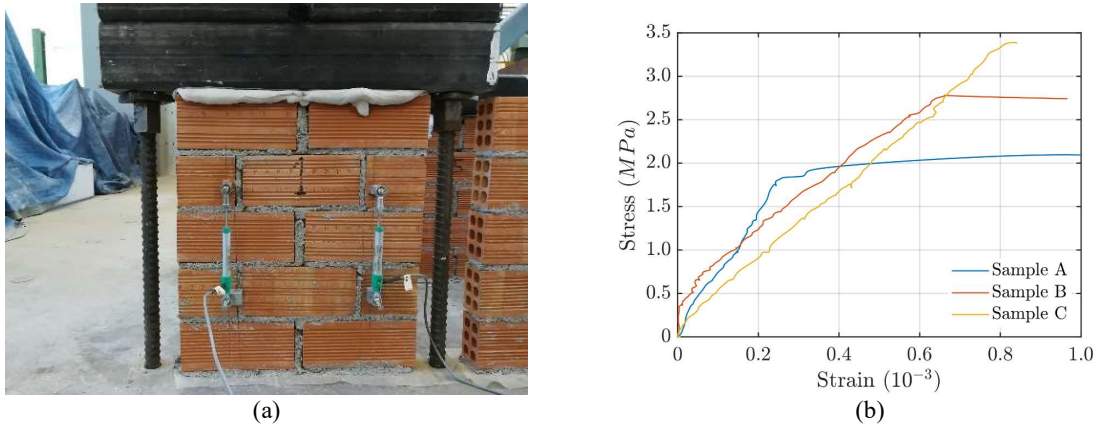


Figure 5. (a) Typical setup for masonry compression test; (b) Strain-stress for different masonry compression test specimens.

298

299

300

Table 8. Maximum compression strength of specimens and corresponding strain.

Specimen	Width	Height	Thickness	Compressive strength	Elastic modulus
	(mm)	(mm)	(mm)	(MPa)	(MPa)
A	392	458	58	2.24	8388.44
B	392	458	58	2.79	9441.62
C	392	457	58	3.41	5174.94
Mean				2.81	7668.33
Standard deviation				0.48	1814.76

301

302

303

Shear test on the infill panels

304 The shear strength was determined through diagonal compressive tests of masonry wall samples according to the ASTM
 305 E519 [52]. Three specimens were tested in the lab, whose dimensions are summarised in Table 9. According to the data
 306 listed in Table 9, the mean shear strength of the masonry wall samples was 0.65 MPa.
 307

308

309

Table 9. Dimensions of the infill sample for the shear test and the shear strength.

Specimen	Force	Width	Height	Thickness	Net area	Shear strength
	(N)	(mm)	(mm)	(mm)	(mm ²)	(MPa)
A	45106	1190	1185	60	47453	0.67
B	44124	1190	1190	60	47552	0.66
C	42398	1183	1192	60	47453	0.63
Mean						0.65
Standard deviation						0.02

310

311

312

313

314

315

316

4 CODE-BASED ASSESSMENT OF THE PROTOTYPE BUILDING USING PUSHOVER ANALYSIS

4.1 Numerical modelling

Modelling of the steel frame

317 3D FE models of both the bare and infilled prototype steel frames were developed in OpenSees [36] in order to conduct
 318 code-based assessment according to the EC8-3. To capture the axial force-bending moment interaction, columns were
 319 modelled with a distributed plasticity fibre-based approach with force-based elements and ten integration points using the
 320 'Steel01' uniaxial material [36] with 2% post-yield hardening (see Figure 6(a)). Conversely, the beams were modelled
 321 using elastic elements with lumped plasticity by introducing non-linear rotational springs at beam ends. The plastic hinges

322 were modelled with zero-length elements, whose properties were initially calibrated using the moment-rotation
 323 relationship proposed by Lignos and Krawinkler [53] and were further modified based on Zareian and Medina [54] (See
 324 Figure 6(b) and Table 10). Connections were considered fully rigid due to the welded connection type and the stiffeners
 325 placed at beam-column joints. Besides, since the tests were performed in the direction along the columns' weak axis, the
 326 flexibility due to the shear behaviour of the column panel zones was neglected. All column base nodes are fixed to the
 327 ground, and a rigid diaphragm is used to simulate the presence of the composite slab. Gravity loads were applied on the
 328 beams by considering the seismic combination of the Eurocode 8 [1], while the storey masses were equally distributed at
 329 the beam-column connections.
 330

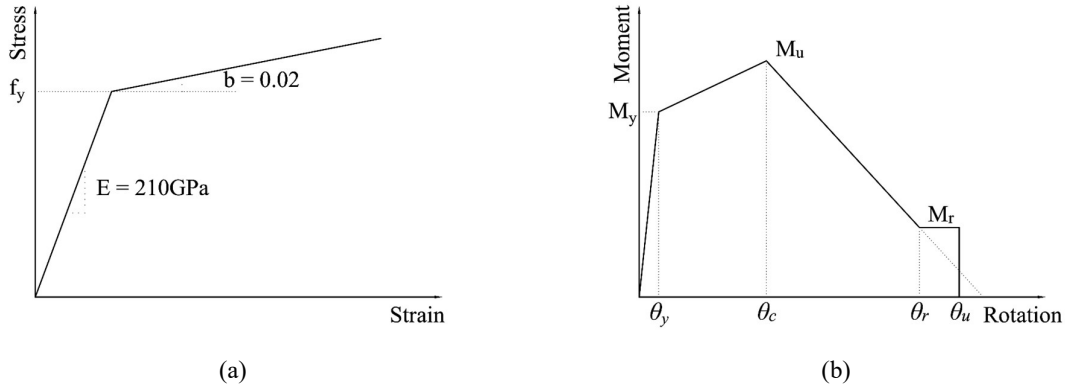


Figure 6. Material properties: (a) S355 steel; (b) Model of the beam plastic hinges (See values in Table 10).

331
 332
 333

Table 10. Parameters defining the backbone curve of beam plastic hinges (See Figure 6(b)).

Yielding		Ultimate capacity		Residual capacity	
M_y	θ_y	M_u	θ_u	M_r	θ_r
(kNm)	(rad)	(kNm)	(rad)	(kNm)	(rad)
201	1.16e-03	216	0.06	86	0.18

334
 335
 336

Modelling of masonry infill

337 In addition, the masonry infill walls were included within the model of the infilled structure, utilising single-strut models.
 338 As mentioned in the introduction, there is currently a lack of specialised single-strut models for steel moment frames;
 339 hence, the backbone curve proposed by Fardis and Panagiotakos 1997 [11], Dolšek and Fajfar 2005 [12] and Liberatore
 340 and Decanini [19] were used and compared in this study, such that their ability to represent infill within steel moment
 341 frames could be evaluated. However, the cyclic behaviour of masonry struts was defined using the same parameters
 342 controlling the pinching and cyclic damage recommended by Mohammad Noh *et al.* [21], as not all of the above three
 343 models explicitly provided a hysteresis rule along with the backbone curve.
 344

345 All the selected single-strut models utilise one compressive strut in each diagonal direction, as shown in Figure 7(a),
 346 which has the same thickness as the real masonry infill wall, and has an effective width related to the factor of relative
 347 stiffness λ_h , as given in Eq. (1):
 348

$$\lambda_h = \sqrt[4]{\frac{E_m t_m \sin(2\theta)}{4E_c I h_m}} h \quad (1)$$

349
 350
 351
 352
 353
 354
 355

which is a function of the elastic modulus of the masonry infills (E_m) and the column (E_c), the height (h_m) and thickness
 (t_m) of infill walls, the angle between the strut and horizontal axis (θ), the second moment of area of columns (I) and the
 storey height (h). Table 11 reports the comparison of the different formulae for the definition of the effective width of
 struts in each selected single-strut model, where d is the diagonal length of the infill wall. The values of coefficient K_1
 and K_2 in Eq. (4) are summarised in Table 12.

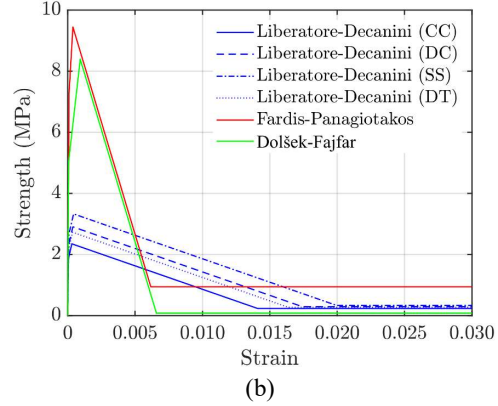
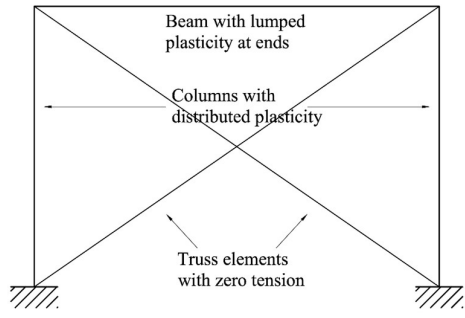


Figure 7. Schematic view of the single strut model for masonry infills and backbone curves.

356
357
358

Table 11. Formulae of effective width used by the single-strut models.

Model	Effective width
Fardis-Panagiotakos	$b_m = 0.175d\lambda_h^{-0.4}$ (2)
Dolšek-Fajfar	$b_m = 0.175d\lambda_h^{-0.4}$ (3)
Liberatore-Decanini	$b_m = \left(\frac{K_1}{\lambda_h} + K_2\right)d$ (4)

359
360
361

Table 12. Values of the coefficient K_1 and K_2 for determining the effective width of masonry struts [17].

	$\lambda_h < 3.14$	$3.14 < \lambda_h < 7.85$	$\lambda_h > 7.85$
K_1	1.300	0.707	0.470
K_2	-0.178	0.010	0.040

362
363
364

Table 13. Formulae of ultimate lateral force used by the single-strut models.

Model	Ultimate lateral force
Fardis-Panagiotakos	$F_m = 1.3\sigma_{m0}t_mL_m$ (5)
Dolšek-Fajfar	$F_m = 0.818 \frac{\sigma_{m0}t_mL_m}{C_I} \left(1 + \sqrt{C_I^2 + 1}\right)$ where $C_I = 1.925 \frac{L_m}{h_m}$ (6)
Liberatore-Decanini	$H_{cc} = \frac{1.12 \sin \theta \cos \theta}{K_1(\lambda_h)^{-0.12} + K_2(\lambda_h)^{0.88}} \sigma_{m0}$ (7)
	$H_{dt} = \frac{0.6\tau_{m0} + 0.3\sigma_0}{b_m/d}$ (8)
	$H_{ss} = \frac{(1.2 \sin \theta + 0.45 \cos \theta)\tau_0 + 0.3\sigma_0}{b_m/d}$ (9)
	$H_{dc} = \frac{1.16 \tan \theta}{K_1 + K_2(\lambda_h)} \sigma_{m0}$ (10)

365
366
367
368
369
370

Another major difference between the Fardis-Panagiotakos model, the Dolšek-Fajfar model and the Liberatore-Decanini model is that the former two determine the strength of masonry struts based solely on the shear failure of masonry infill. Conversely, the latter considers four different damage patterns of masonry infill panel, namely corner crush (CC), diagonal tension (DT), sliding shear (SS) and diagonal compression (DC) damage pattern. The formulae used to determine the ultimate lateral force of masonry strut are summarised in Eqs. (6) to (10), where σ_{m0} and τ_{m0} are the vertical

371 compression strength and shear strength, respectively obtained from the compression tests and diagonal compression tests
 372 in Section 3.2, σ_0 is the total vertical stress due to gravity load, and lastly τ_0 is the slide resistance assuming 70% of the
 373 shear strength τ_{m0} . The backbone curves used by the three single-strut models are summarised in Figure 7(b). It can be
 374 concluded that the Fardis-Panagiotakos model and the Dolšek-Fajfar model assumed much higher strength of the masonry
 375 strut than the Liberatore-Decanini model. Besides, the former two models also estimated a slightly higher initial stiffness
 376 of the struts than the Liberatore-Decanini model. Lastly, in the Liberatore-Decanini model, the strength corresponded to
 377 the least critical damage pattern (sliding shear) was approximately 50% higher than the strength corresponded to the most
 378 critical damage pattern (corner crush).

379
380 Table 14. Modal characteristics of the prototype building.
381

		1 st mode period T ₁ (sec)	2 nd mode period T ₂ (sec)	1 st mode shape
Bare Frame		1.207	0.435	[0.50, 1]
Infilled Frame	Liberatore-Decanini	0.088	0.035	[0.54, 1]
	Fardis-Panagiotakos	0.079	0.031	[0.53, 1]
	Dolšek-Fajfar	0.079	0.031	[0.53, 1]

382 Table 14 provides the dynamic features, *i.e.*, periods and mode-shape in the x -direction, obtained by the numerical model
 383 of both the bare and infilled configurations of the prototype building. It is noteworthy that the Fardis-Panagiotakos model
 384 and the Dolšek-Fajfar model provided the same results since they adopted the same initial stiffness in the modelling of
 385 masonry struts. The periods obtained by the Liberatore-Decanini model was slightly longer than the periods obtained
 386 from the other two models. The modal properties were used in the following code-based assessment of the prototype
 387 building using pushover analysis approach.
 388
 389

390 4.2 Code-based assessment of the prototype building

391
 392 The seismic performance of the case-study structure was assessed according to the EC8-3 and pushover analysis methods.
 393 Procedures based on linear analysis methods were not considered in this study. In agreement with the experimental tests,
 394 only the x -direction (see Figure 2) was considered during the assessment. The member rotation capacities proposed in
 395 the EC8-3 [9] were adopted as acceptance criteria, which are $0.25\theta_y$, $2\theta_y$ and $3\theta_y$ respectively for the DL, SD and NC limit
 396 state, as the sections used are class 2 cross-sections according to EC3 [47]. The yield rotation of columns θ_y in this study
 397 was 0.0163 rad, which was calculated according to the formula in the latest American code ASCE41-17 [56] which can
 398 be simplified as follow:
 399

$$\theta_y = \frac{M_{pl,Rd}L}{6EI} \left(1 + \frac{12EI}{L^2GA_s} \right) \quad (11)$$

400 where $M_{pl,Rd}$ is the moment capacity of column, L is the length of the column, E and G are respectively the Young's
 401 modulus and shear modulus, I is the second moment of area and A_s is the shear area of column cross-section.
 402
 403

404 The non-linear static behaviour of both the bare and infilled prototype building was investigated performing pushover
 405 analyses in accordance with the EC8-3, and considering two load patterns: (i) the 'modal' pattern, where the lateral force
 406 is proportional to the mass and the first mode of vibration; (ii) the 'uniform' pattern, where the lateral load is proportional
 407 to mass at each storey. Since the two load patterns led to very similar results, only those based on the 'modal' load pattern
 408 are presented in Figure 8. It can be seen that due to the 'special' shape of the pushover curves of infilled frames, the N2
 409 method [46] recommended by EC8-3 was not appropriate for the case of infilled frames. To this end, a new version of
 410 the N2 method [57], which was proposed especially for infilled structures, was adopted in this paper for dealing with the
 411 effects of masonry infill. Following the procedure of the N2 method for bare frames [46] and infilled frames [57], Figure
 412 8(a) shows the equivalent linearised pushover curves (bi-linearisation and multi-linearisation for the bare and infilled
 413 frame), and Figure 8(b) presents the original pushover curves with the indication of seismic demands and capacities for
 414 all limit states and detailed data provided in Table 15. Only the N2 method for bare frames is included in the current
 415 version of EC8-3, so the use of N2 method for infilled frames was not strictly standardised. Nevertheless, the latter was
 416 still necessary, as the shapes of pushover curve of the infilled frame were not suitable for bi-linearisation, hence the
 417 conventional N2 method was not applicable to the infilled frame in this study.
 418

419 It can be seen in Figure 8 that the bare frame exhibited an ultimate strength slightly larger than 500 kN, and was
 420 considered unsafe for both the DL and SD limit state. In the case of infilled frames, it is demonstrated in Figure 8
 421 that the pushover curves obtained by the three approaches of masonry struts differed significantly from each other. In

422 alignment with the backbone curves of masonry struts in Figure 7(b), the Fardis-Panagiotakos model provided the largest
 423 estimate of ultimate strength of the prototype building, which was 2766 kN at 0.07% roof drift ratio, while the Liberatore-
 424 Decanini model had the lowest ultimate strength, which was 1115 kN at 0.04% roof drift ratio. The ultimate strength
 425 provided by the Dolšek-Fajfar model was 2497 kN at 0.13% roof drift ratio. Despite the considerable differences between
 426 the pushover curves, the three approaches achieved good agreement in terms of the seismic demands and capacities, as
 427 illustrated in Table 15. In general, the presence of masonry infill was beneficial to the resistance of the prototype building.
 428 The points of seismic demand were all at smaller top storey drifts than their corresponding points of capacity, hence the
 429 infilled frame was considered to fulfil the performance requirements of all limit states defined in EC8-3. Nevertheless,
 430 the presence of masonry infills also reduced the displacement capacity of the case study building by 48, 40 and 33%,
 431 respectively, for DL, SD and NC limit state, compared to the capacity of the bare frame. The reduction in the displacement
 432 capacities was due to the soft storey mechanism at the first storey, whose capacity dominated the overall capacity of the
 433 infilled steel building.
 434

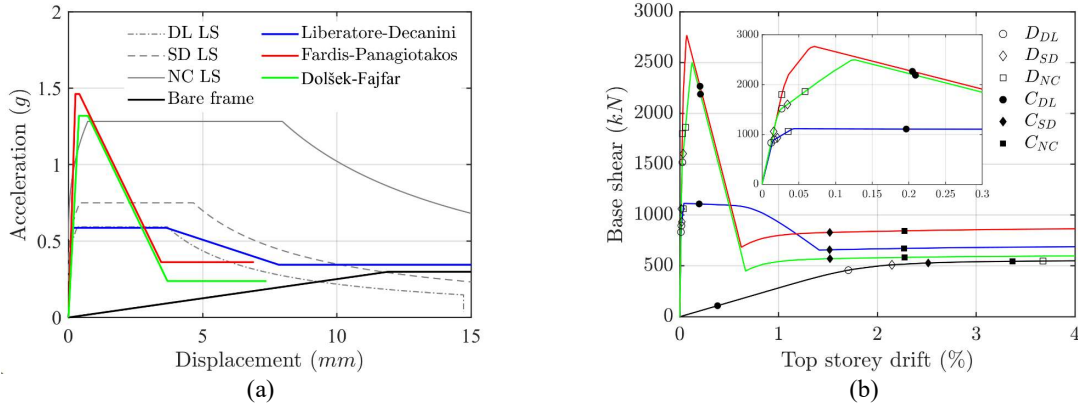


Figure 8. Pushover curves of the bare and infilled prototype building: (a) Implementation of the N2 methods; (b) Capacity curves with seismic demands (D) and capacities (C).

435
 436
 437

Table 15. Demands and capacities of the prototype building in terms of roof drifts (%).

		DL		SD		NC	
		Demand	Capacity	Demand	Capacity	Demand	Capacity
Bare frame		1.700	0.382	2.153	2.515	3.681	3.368
Infilled frame	Liberatore-Decanini	0.016	0.197	0.021	1.516	0.035	2.271
	Fardis-Panagiotakos	0.012	0.204	0.016	1.519	0.026	2.274
	Dolšek-Fajfar	0.026	0.209	0.034	1.521	0.059	2.275

438
 439
 440
 441
 442
 443
 444
 445
 446
 447
 448
 449
 450
 451
 452
 453
 454
 455
 456

It can be concluded, based on the above-standardised assessment of the prototype building, that the presence of masonry infills had a significant impact on the seismic performance of the steel frame, which, however, is not properly accounted for in the current EC8-3 [1]. Firstly, the standardised N2 method [46] for determining the displacement demands is not appropriate considering the ‘special’ shape of the pushover curves for infilled structures, as shown in Figure 8. Besides, there is also a lack of accurate guidance on how to model the masonry infills in EC8-3, in terms of both the geometry and mechanical property, as well as compliance criteria regarding the capacity of masonry infills. Lastly, the current modelling of infilled frames showed significant differences of the order of 50% in terms of estimated ultimate strength, which needs further investigation by comparing with experimental tests.

5 PSEUDO-DYNAMIC TESTS

This section presents the numerical simulation of the PsD tests of the case-study steel MRF carried out in the STRULAB. The test frame was the central bay of the 75% scaled prototype building. The test matrix is summarised in Table 16. The test frame was first subjected to a modal characterisation process through snap-back free vibration tests for the bare and infilled configurations to allow the numerical models’ calibration. The test frame was successfully subjected to an incremental PsD test under seismic sequences of three ground motions, considering scaling factors for the ground motion intensity (SF), respectively equal to 1.0 and 3.0. It is worth mentioning that the SF equal to 3 was chosen to ensure the structure’s failure under the ground motion sequence with this intensity.

457
458
459

Table 16. Test matrix for the 3D scaled bare and infilled frame in the laboratory.

Test	Description
1	Snap-back free-vibration test of the bare frame
2	Snap-back free-vibration test of the infilled frame
3	PsD test of the infilled frame with the first component of earthquake sequence (SF=1)
4	PsD test of the infilled frame with the full earthquake sequence (SF=1)
5	PsD test of the infilled frame with the full earthquake sequence (SF=3)

460
461
462
463
464

For safety issues, in the laboratory, the last test with SF of 3.0 was terminated when the inter-storey drift ratio (IDR) reached 5%. After each ground motion of the sequence for the different sequence intensities, small harmonic excitations were applied to the structure in order to evaluate the variation of the vibration periods, *i.e.*, period elongation, along with the test.

465
466
467

5.1 Selection of ground motion sequence

468
469
470
471

Three ground motion records, defining the ground motion sequence, were selected in order to: (i) be representative of moderate-to-high seismicity in some areas of Southern Europe; (ii) have large spectral accelerations in the range of natural period of the case-study frame in the different configurations, *i.e.*, 0.1 to 0.9 sec, respectively, for the infilled frame and for the bare frame of the full-scale three-bay case-study structure.

472
473
474
475
476
477
478
479
480

Table 17 summarises the basic information of the selected earthquakes, including date, moment magnitude (M_w) and epicentral distance (R_{epi}) of the seismic event and the peak ground acceleration (PGA) of the recorded acceleration time-histories. To reflect the variation of the dynamic properties due to the scaling, the time step of the ground motion sequence, which was originally 0.02 sec, was scaled by a factor of 0.87 (the square root of 0.75) to 0.0173 sec, while the amplitudes remained the same as no scaling was required for the acceleration (see Table 3). Additional information is provided in Figure 9 that displays the time history of the earthquake sequence. Figure 10 shows the response spectra of each individual ground motion, as well as the comparison with the elastic response spectrum defined by EC8-3 at the SD and NC limit states.

481
482
483
484
485
486
487
488
489
490

The three selected ground motions considered in this study referred to the 2016 Central Italy earthquakes recorded at the Station in Norcia (NRC) in the East-West component. The acceleration time-histories were available from the Engineering Strong-Motion database (ESM) [55]. The foreshock has a PGA of 0.35g, the mainshock has a PGA of 0.48g, which is the largest PGA of the whole sequence, while the aftershock has the smallest PGA of 0.30g. As shown in Figure 10(a), within the range from 0.2 times the fundamental period of the infilled frame to two times the fundamental period of the bare frame, the response spectra of the unscaled ground motions were close to the elastic response spectrum of SD limit state, with ground motion 1 (GM1) and ground motion 3 (GM3) being slightly lower while ground motion 2 (GM2) being slightly higher. On the other hand, Figure 10(b) shows the same comparison at NC limit state. In this case, the response spectra of scaled ground motions were higher than then codified elastic response spectrum.

491
492
493

Table 17. Seismic sequence: selected ground motion records.

Event	Date & Hour	M_w (-)	R_{epi} (km)	PGA (g)	ID
GM1	24/08/2016 at 1.36	6.0	15.3	0.35	EMSC-20160824_0000006
GM2	30/10/2016 at 6.40	6.5	4.6	0.48	EMSC-20161030_0000029
GM3	26/10/2016 at 17.10	5.4	9.4	0.30	EMSC-20161026_0000077

*Station in Norcia, Italy (NRC) and East-West component of the ground motion. Source: <https://esm.mi.ingv.it/>

494

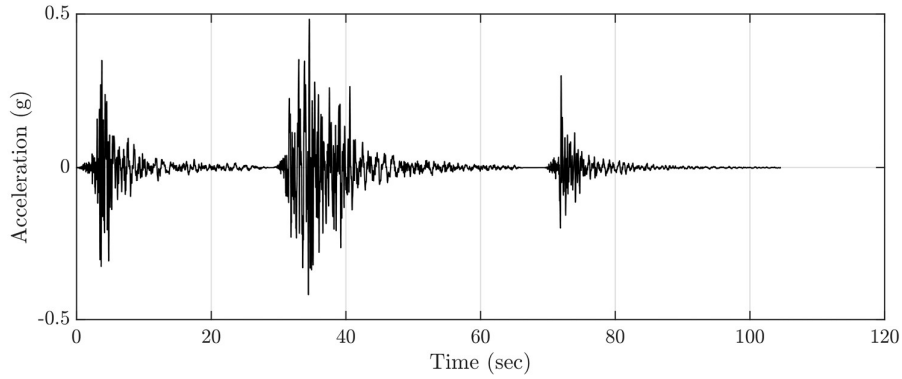


Figure 9. Time history of the seismic sequence.

495

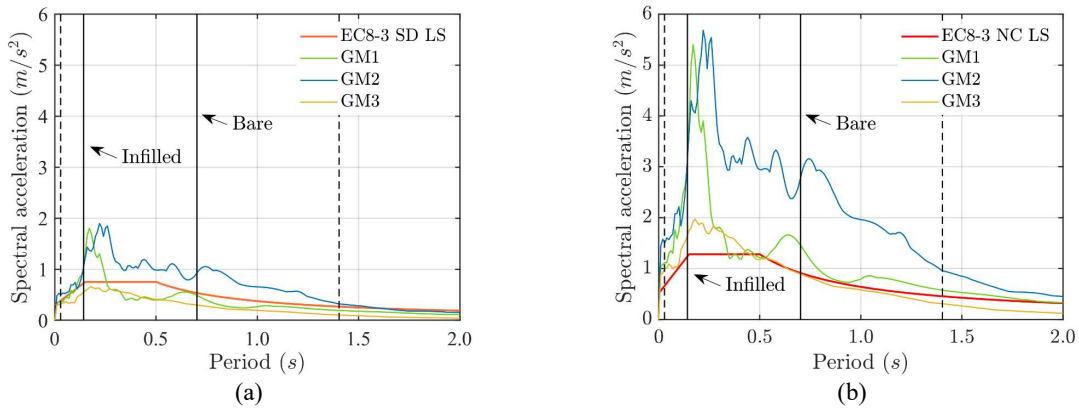


Figure 10. Comparison of the response spectra of selected ground motions with the elastic response spectrum suggested in EC8-3: (a) Unscaled ground motions at significant damage limit state; (b) Scaled ground motions at near collapse limit state.

496

497

498

499

500

501

502

503

504

505

506

5.2 Experimental setup and instrumentation

The setup of the 3D test is shown in Figure 11. The tested structures were designed and built based on the common European constructional practice. Therefore, the steel frames were welded and prepared in the workshop and fully assembled on-site (*i.e.*, in the lab for this case). Two parallel tubular beams were placed on top of each steel base plates and anchored to the strong floor of the lab in order to increase the rigidity of the base restraints of the mockup. The composite slab was built following the erection of the bare steel frame. Indeed, the corrugated steel sheetings were installed on the beams and once fixed with the shear connectors. The concrete constituting the slab was cast and poured on-site.



(a)



(b)

Figure 11. Layout of the setup used for the 3D structure.

507 Concerning the installation of actuators, two post-tensioned steel bars were located at each connection with the actuators
 508 to control the deformation of the specimen. Two actuators were placed at each storey, connected to the reaction wall, as
 509 shown in Figure 12. Once the concrete had set, additional pre-cast concrete blocks were added on each floor to simulate
 510 the gravity loads imposed on the structure (see Figure 11), which influences the columns' plastic rotation and the
 511 asymmetrical moment and shear forces on the beams. The additional concrete blocks were divided into two groups, one
 512 representing the equivalent weight of the non-structural permanent loads and the imposed loads, excluding the self-weight
 513 of masonry infills, which is 12.50 and 10.15 tons for the first and top storey, and the other one representing the self-weight
 514 of masonry infills, which is 1.01 and 0.51 tons for the first and top storey. These concrete blocks of masonry infills were
 515 removed after the actual masonry walls were built. However the concrete blocks represented only the theoretical mass of
 516 masonry infills and the real mass of infills was measured to be 2.03 and 0.99 tons for the first and top floor. Modal analysis
 517 showed that such small differences had negligible influence on behaviour of the test mockup. Finally, the masonry wall
 518 panels were built in two layers and using local construction practice.

519
 520 The instrumentation for the PsD tests was designed to monitor the response of several structural components, however,
 521 only those relevant to this study are described here and are summarised in Table 18. Apart from the accelerometers used
 522 in the free vibration tests (Figure 12(a)), a total of four displacement-measuring optical devices were utilised in the test
 523 to monitor storey displacements, with two at each storey, whose locations are demonstrated in Figure 12(a) as well.
 524 Furthermore, 16 strain gauges were also utilised to measure the strains induced in columns and beams, whose locations
 525 are shown in Figure 12(b). It can be seen that the measurement of strain primarily focused on the steel components at the
 526 first storey, which was decided on the basis of the number of strain gauges available during the test.
 527

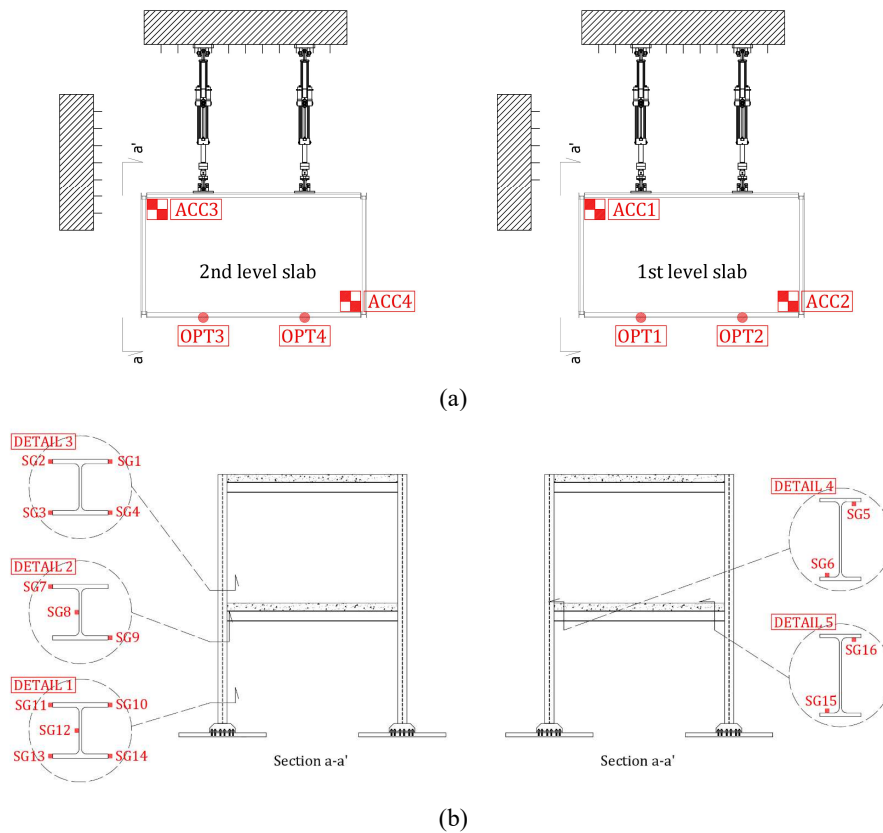


Figure 12. Locations of actuators and sensors on the 3D scaled steel frame.

528
 529
 530

Table 18. The list of sensors and devices used for the PsD tests (See Figure 19 for locations).

Label	Device	Descriptions	Quantity
ACC	Accelerometer	ACC1-2: acceleration of first storey (free vibration tests only). ACC3-4: acceleration of top storey (free vibration tests only).	4
OPT	Optical device	OPT1-2: displacements of first storey in the test direction. OPT3-4: displacements of top storey in the test direction.	4
SG	Strain gauge	SG1-4 and 7-14: strain in columns SG5-6 and 15-16: strain in beams	16

531
532
533
534
535
536
537
538
539
540
541

5.3 Numerical modelling of the test mockup

3D FE models of both the bare and infilled configurations of the test frame were also developed in OpenSees [36]. The modelling procedure followed the same approach described in Section 3.2 as per the prototype frame. As summarised in Table 16, snap-back free-vibration tests were firstly performed on the bare (*i.e.*, ‘Test 1’) and the infilled frame (*i.e.*, ‘Test 2’) for comparison of the initial stiffness and natural periods. At the beginning of each snap-back test, the structure was pulled at the top storey through a rod with reduced section, as demonstrated in Figure 13, which broke at a certain predefined level of load, allowing the sudden release of force and free vibration of the tested frame. The forces applied to the bare frame and the infilled frame were 26 and 62 kN, respectively.



Figure 13. The apparatus for the snap-back free-vibration test (a); details of the rod with reduced section (b).

542
543
544
545
546
547
548
549
550
551
552
553
554
555
556

Figure 14 shows the time-history of the mean top floor displacement of the test frame. It can be seen that despite a larger initial force was applied to the infilled frame, the consequential displacement induced at the top floor of the infilled frame was much smaller compared to the case of bare frame, due to the higher lateral stiffness of the infilled frame. Also, the infilled frame’s vibration decayed much faster than the bare frame, indicating higher damping caused by the presence of infills. Figure 15 shows the profiles of initial lateral displacements of the test frame obtained numerically and experimentally for the purpose of calibrating the numerical model based on initial stiffness. It is clear that the initial displacement profile of the bare frame achieved a good match with the experimental results, as shown in Figure 15(a), where the differences were smaller than 5% according to Table 19. On the other hand, the comparison of the infilled frame’s initial displacement is shown in Figure 15(b), where it can be seen that the numerical model had a much larger initial stiffness than the lab specimen, as the initial displacements obtained from all three models were significantly underestimated by approximately 60% at both storeys. Given the good match of the numerical and experimental results for the bare frame, the infilled frame’s higher initial stiffness has to be attributed to the overestimated initial stiffness of the adopted masonry infills models.

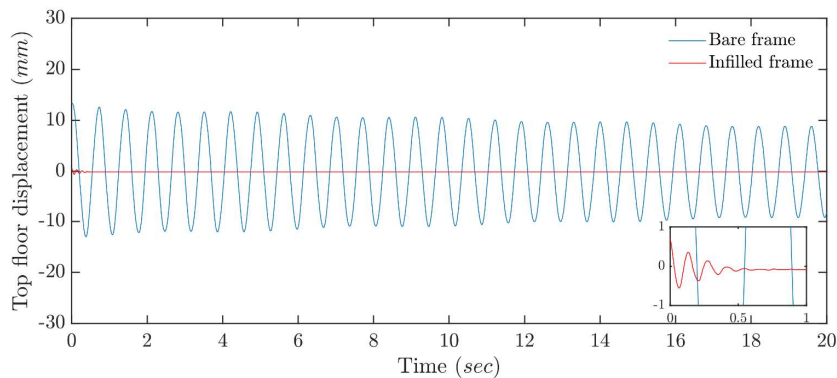


Figure 14. Time-history of top floor displacement of the test frame obtained from snap-back tests.

557

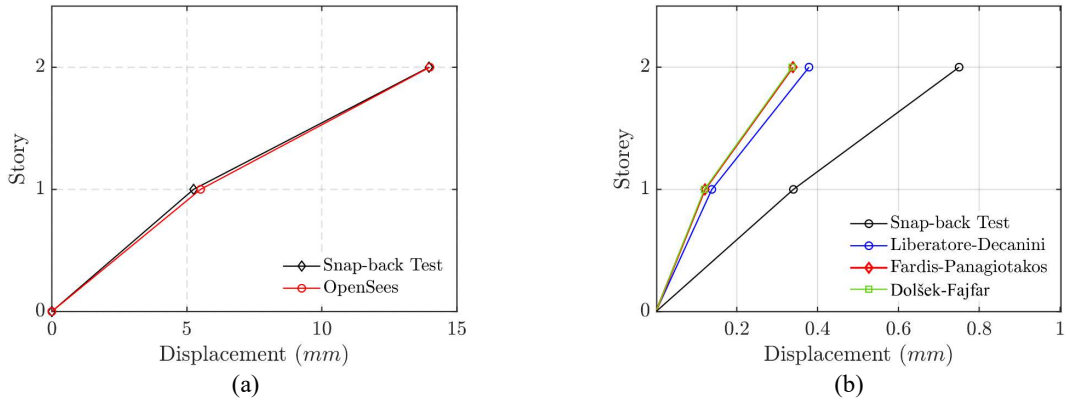


Figure 15. Initial displacements induced by actuators: (a) bare frame and (b) infilled frame.

558
559
560

Table 19. Initial displacement of the test frame during the snap-back test (unit: mm).

		Snap-back test		OpenSees			
		First floor	Top floor	First floor		Top floor	
Bare frame		5.25	13.97	5.51	4.95%	14.00	0.21%
Infilled	Liberatore-Decanini	0.34	0.75	0.14	-58.82%	0.38	-49.33%
	Fardis-Panagiotakos			0.12	-64.71%	0.34	-54.67%
	Dolšek-Fajfar			0.12	-64.71%	0.34	-54.67%

561

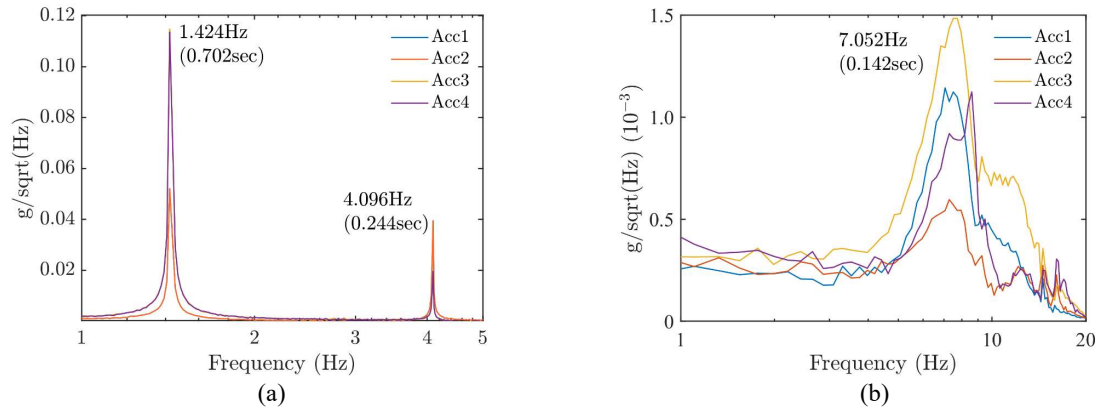


Figure 16. Power spectral density: (a) the bare frame; (b) the infilled frame (low-pass filter applied at 20Hz).

562
563
564

Table 20. Periods of vibration and damping ratios of the tested mockup from free-vibration tests.

Configuration		1 st mode			2 nd mode		
		Period (sec)		Damping	Period (sec)		Damping
		Test	OpenSees	Test	Test	OpenSees	Test
Bare frame		0.702	0.699	0.2%	0.244	0.243	0.1%
Infilled frame	Liberatore-Decanini	0.142	0.077	10.0%	N/A*	0.026	N/A*
	Fardis-Panagiotakos					0.072	
	Dolšek-Fajfar					0.072	

* The second mode cannot be identified from the PSD in Figure 16.

565
566
567
568
569
570

Figure 16 shows the power spectral density obtained from the free-vibration tests from which the natural periods were extracted, while Table 20 reports both the natural periods obtained from the free-vibration tests and those from numerical analyses. A total of 4 accelerometers were employed for the tests, whose location is represented in Figure 12. According to Figure 16(a), the power spectral density for the bare frame exhibited clear peaks for the first two global modes. On the

571 other hand, the infilled frame's response exhibited only the peak of the fundamental mode, as a very small initial
572 amplitude, *i.e.*, less than 1 mm, was applied at the top of the infilled frame, providing limited data for modal identification.
573 Additionally, the presence of masonry infills might have resulted in uneven lateral stiffness of the entire structure, as
574 shown in Figure 16(b), where the accelerometers on the same storey reached different peak amplitudes. Lastly, the
575 periods extracted from the free-vibration test are summarised in Table 20. It is shown that the periods obtained from the
576 numerical model of the bare frame matched well the experimental observations, with discrepancies less than 1%.
577 However, the fundamental periods of the infilled frame's numerical model are much shorter than the period of the infilled
578 frame obtained from the test, thus indicating the higher stiffness of numerical models of masonry infill.

579 5.4 Damage observed on the masonry infill walls

582 The following sections present the numerical and the experimental results of the PsD tests performed on the 3D infilled
583 test frame with a higher focus on infill walls' response. The numerical and experimental results were presented together
584 for direct comparisons in order to identify the gaps between available FE modelling strategies and real infilled steel MRFs.
585 According to the experimental program, the PsD tests comprised three parts, which were referred to as 'Test 3', 'Test 4'
586 and 'Test 5' (see Table 16).

588 During 'Test 3', the infilled frame was subjected to the first component of the earthquake sequence with SF equal to 1.
589 The damage was firstly observed at the top corners of infill walls next to the beam splice connections, where the interlock
590 between the bolts and the top layer of bricks created a strut at the corner, resulting in local crush around the bolts and
591 cracks at corners, as shown in Figure 17 and demonstrated in Figure 18. The cracks were originated from the bolts in the
592 beam splice connections and propagated along the bricks' surface to the edge of the infill wall panel. This damage at top
593 corners must be distinguished from the corner crush damage pattern, one of the most common damage modes on infill
594 walls summarised in literature [58], where the strut formation is corresponding to the entire infill wall panel, hence cracks
595 normally occur at both corners, *e.g.*, top-right and bottom-left, in the diagonal direction.

596

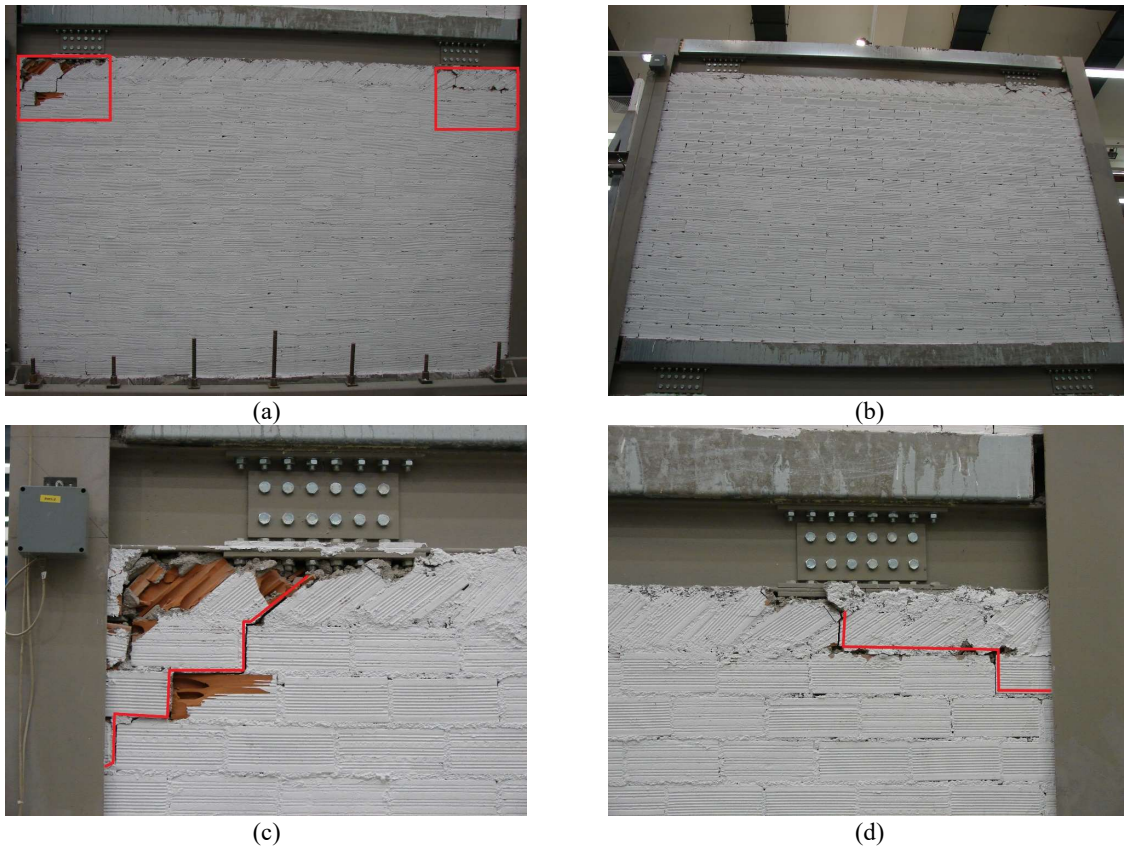


Figure 17. Damage observed on the infilled steel frame during 'Test 3' and 'Test 4': (a) first floor infill wall; (b) top floor infill wall; (c) detail of cracks at the top left corner; (d) detail of cracks at the top right corner.

597

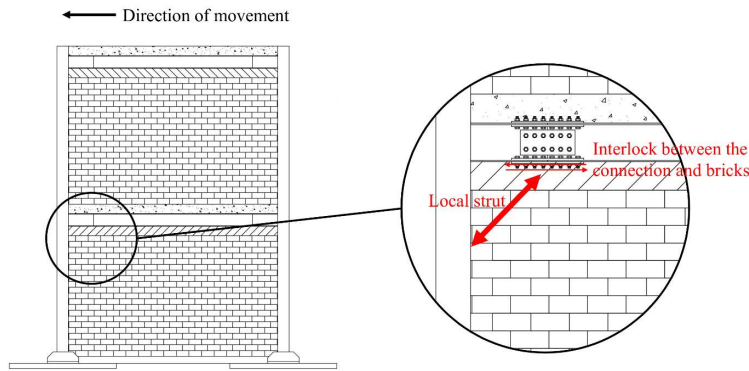


Figure 18. Demonstration of the formation of local struts near the beam splice connection.

598
599
600
601
602
603
604
605

During ‘Test 4’, the infilled frame was subjected to the entire earthquake sequence with SF equal to 1, yielding an increase in the infills’ damage with respect to the previous ‘Test 3’. However, it is anticipated that the restraint imposed by the column flanges in the out-of-plane direction of the masonry infills prevented the immediate out-of-plane failure of the walls following the local crushing and cracking at corners, as may happen in the case of a RC column. No significant yielding was observed on steel members, which will be demonstrated by strain measurement in the following section, so the damage on steel members was considered limited at this stage.

606
607
608
609
610
611
612
613
614
615
616
617
618

During ‘Test 5’, where the structure was subjected to the earthquake sequence with SF equal to 3, significant drifts were observed at both the first and top floor, and the test was terminated during the second ground motion component when the IDR was approaching 5%. For the masonry infills, the crush at top corners became larger with some bricks falling onto the ground. Also, three additional damage pattern were observed on the infill walls, which were similar to what typically occurs to the infill walls in RC structures namely: (i) the diagonal cracks due to tension, (ii) the sliding shear at mid-height of wall, and (iii) the diagonal compression mode leading to out-of-plane failure (which is due to the slenderness of the wall). Initially, the diagonal crack occurred only at the central part of the infill wall, as shown in Figure 19(a), but a horizontal crack subsequently developed at approximately mid-height of the wall, together with out-of-plane deformation of the wall, as shown in Figure 19(b). Besides the damage on the infill walls, significant yielding was also observed at columns, particularly near column base and beam-column joints, as highlighted in Figure 19(c) and (d). Lastly, it should be noted that at the top floor, only the cracks at top corners and diagonal cracks were observed on the infill walls, so the damage was considered limited compared to the severe damage at the first floor.

619
620

Table 21. Strength associated with different damage patterns in the Liberatore-Decanini model.

Damage pattern	Corner crush	Sliding shear	Diagonal tension	Diagonal compression
Strength (MPa)	2.33	3.06	2.56	2.81

621



(a)



(b)



Figure 19. Damage pattern on the infilled steel frame during Test 5: (a) diagonal cracks; (b) combination of corner cracks, diagonal cracks and sliding shear damage pattern (c) yielding at column base (see the flange buckling pointed out by the red arrow); (d) yielding at beam-column joint (see the bending deformation of the column flange in the test direction highlighted by the red arrow).

622

623

624

625

626

627

628

629

630

631

632

633

634

635

636

637

638

639

640

Based on the observation during the PsD tests, it can be concluded that four types of damage patterns were observed on the masonry infill walls, which occurred with the following sequence: (i) cracks at top corners, (ii) diagonal cracks, (iii) sliding shear and subsequently (iv) out-of-plane collapse. The approximate time of occurrence of the damage on infill walls was also marked in the time history of displacement in Figure 20. Table 21 shows the strength associated with different damage patterns according to the Liberatore-Decanini model. It is noticed that, although theoretically would be the first to appear, the corner crush damage pattern was not observed since all the bottom corners of infill walls were not damaged. This is probably due to local struts' formation at top corners, which caused local cracks and crushing, preventing the struts' formation along the original diagonal of infill wall panels, hence protecting the bottom corners from being damaged. The diagonal cracks in Figure 19(a) and (b) can also support this explanation, as they were off the original diagonal of the infill wall. Besides, a sliding shear pattern occurred before any out-of-plane deformation of the infill walls was noticed, while theoretical values show that sliding shear was supposed to be the last damage pattern to occur. This again could be due to the local crush at top corners that prevented the formation of global struts and delayed the occurrence of other damage patterns to different extents. Another reason could be due to the restraint imposed by the flange of columns on the out-of-plane deformation of the infill wall, which could also increase the strength associated with the diagonal compressive pattern.

5.5 Seismic performance of the steel frame with masonry infills

641

642

643

644

645

646

647

648

649

650

651

652

The measured data of structural response during the PsD tests are presented in this section, along with comparisons between numerical and experimental results. Since the restoring forces and deformations at each time step at each storey were the only global response parameters measured during the PsD tests, the numerical model of masonry infills was evaluated mainly based on the comparison of these values from the numerical analyses and PsD tests. The numerical simulations have been performed by applying the same displacement history recorded during the experimental tests, which allowed direct comparisons of the base shear to assess the modelling of infilled frames, however, applying the acceleration quantities in the numerical models would lead to significantly different results, which depended on several parameters, *i.e.*, the hysteresis rule of the model, damping ratios, etc. Besides, according to the results of the code-based assessment of the prototype building and the results of the model calibration of the test frame, the Fardis-Panagiotakos model and the Dolšek-Fajfar model were found to provide similar results; therefore, the Dolšek-Fajfar model was not included in the comparisons in this section.

653

654

655

656

657

658

659

660

661

662

663

664

Figure 20 shows the time-history of IDR at both storeys of the tested frame during each PsD test session. The test frame was only slightly damaged after 'Test 3' and 'Test 4', as indicated by the negligible permanent drifts at both storeys (see Figure 20(a) and (b)). The peak IDR was 0.33% and 0.25% for the first and top storey during 'Test 3', and was 0.30% and 0.32% during the first component of 'Test 4', where only a small increment was observed. During the second component of 'Test 4', the peak IDR was raised to 0.63% and 0.57%, respectively, for the first and top storey, which were approximately twice the peak IDR with respect to the previous ground motion's component. Subsequently, during the last component of 'Test 4', the peak IDR was 0.34% and 0.48% for the first and top storey, respectively. A soft-storey mechanism at the first floor did not occur as expected at this stage, where the displacement at both storeys was very similar to each other during both 'Test 3' and 'Test 4'. This was due to the fact that the damage on the masonry infill was very limited and similar at both storeys, where only cracks at the top corners of each wall were noticed. During 'Test 5', the structure was subjected to up-scaled earthquake records with SF=3, and significant drifts were observed at both the first and top storeys (see Figure 20(c)). The peak IDRs during the first ground motion's component of 'Test 5' were 1.24%

665 and 0.84% respectively at the first and top storey, which were more than three times the peak IDR during its counterpart
 666 in 'Test 4'. Eventually, the PsD test was terminated during the second ground motion of 'Test 5', when the IDR of the
 667 lab specimen was approaching 5%. In this case, it can be seen from Figure 20(c) that the lateral displacement at the first
 668 floor became evidently more significant than the displacement at the top floor, particularly during the second ground
 669 motion when the collapse of the first floor infill wall happened. Therefore it can be anticipated that a severe soft storey
 670 mechanism would occur at the first storey of the test frame if the test continued, particularly when the infill on the ground
 671 was about to fail and collapse, as shown in Figure 19(b).
 672

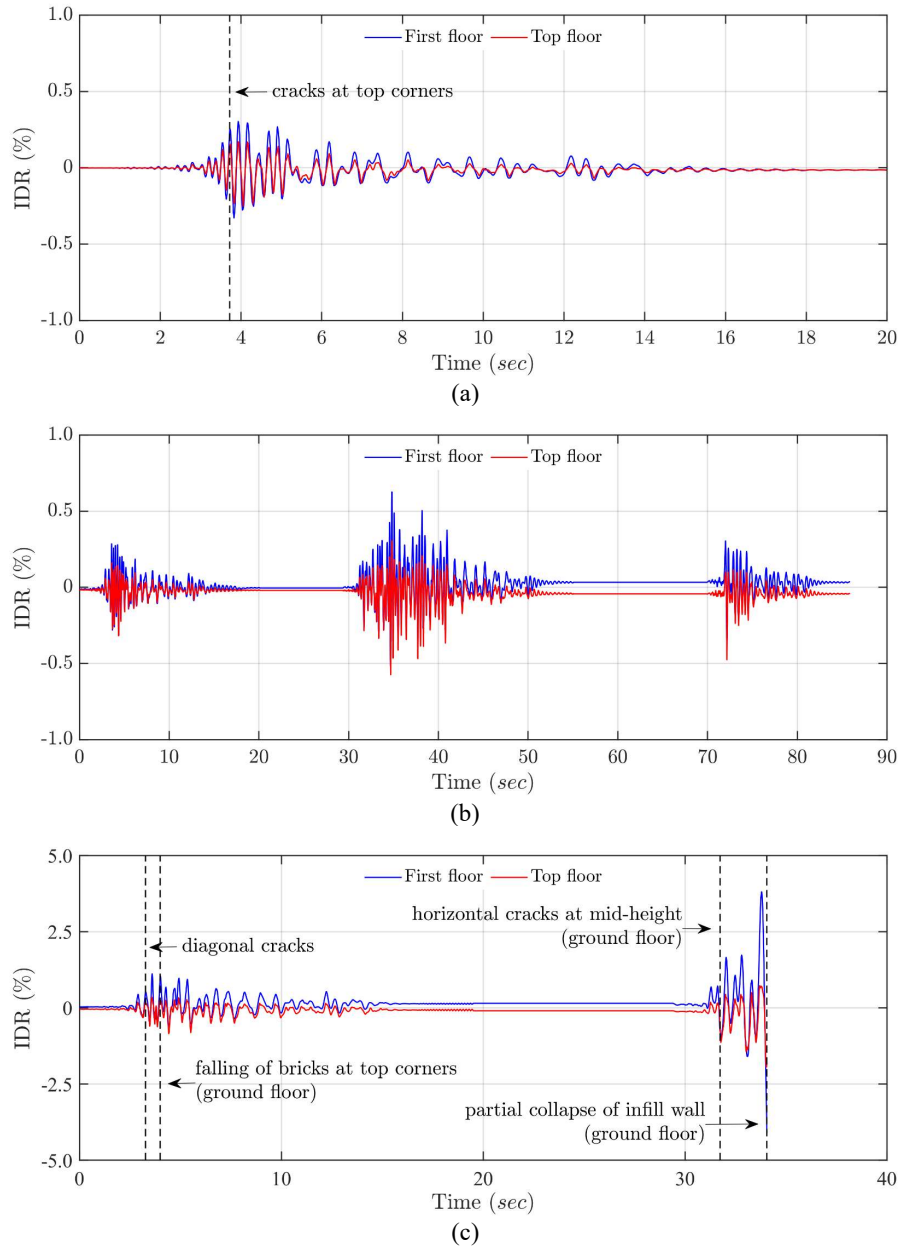


Figure 20. Displacements recorded at both storey of the tested frame: (a) 'Test 3'; (b) 'Test 4'; (c) 'Test 5'.

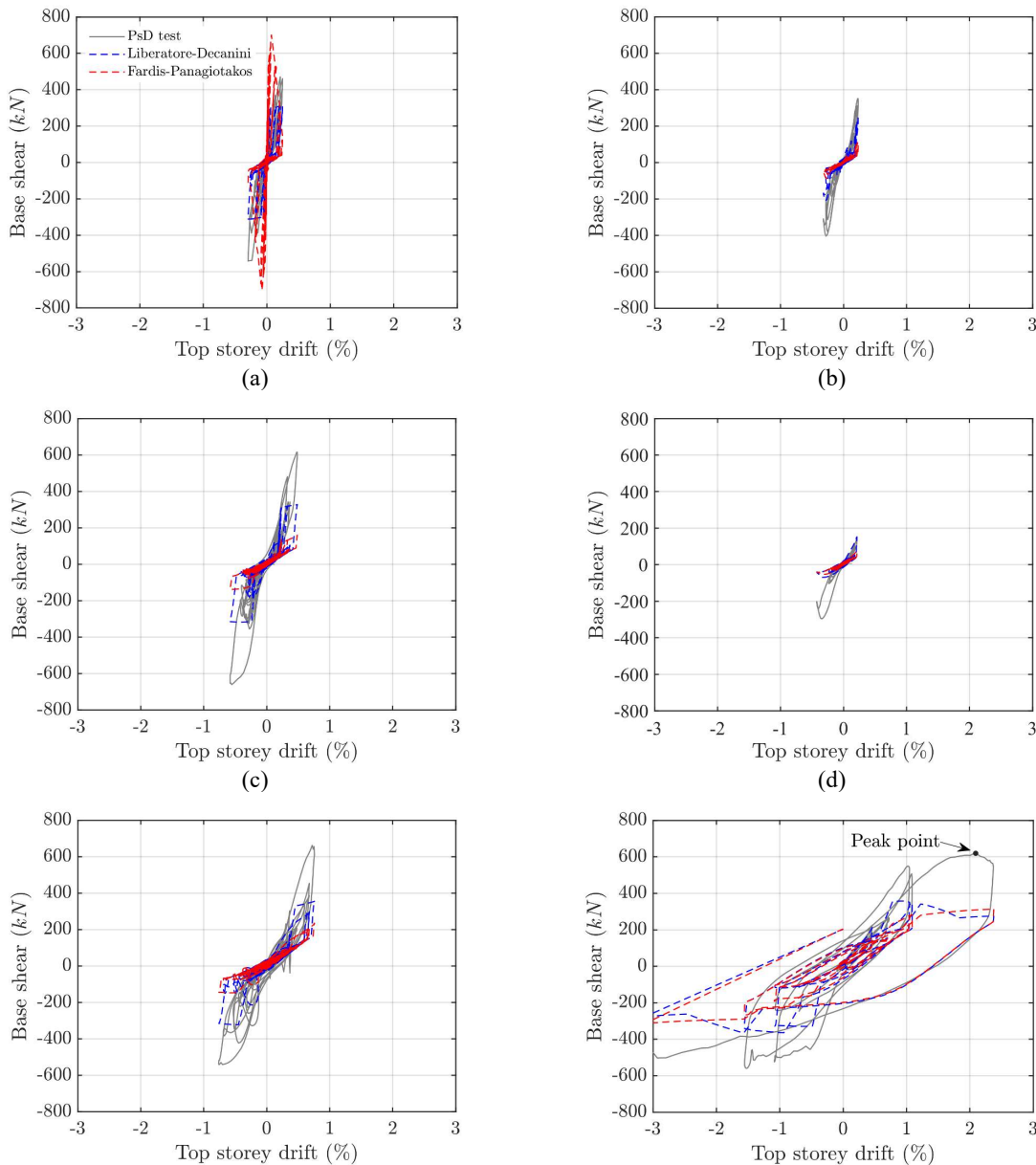
673
 674 Figure 21 shows the comparison between the experimental and numerical cyclic response of the infilled frame, and Table
 675 22 contains comparison of peak base shear obtained numerically and experimentally. The experimental results indicated
 676 that during 'Test 3', 'Test 4' and the first ground motion's component of 'Test 5', the mockup experienced little plastic
 677 behaviour despite the slight pinching effects due to the opening and closing of the cracks at the top corners of infill walls.
 678 Then during the last ground motion's component, the mockup experienced large plastic deformation and exhibited
 679 significant pinching effects, as new cracks occurred and existing cracks became wider. According to the structural
 680 response in Figure 21(c), (e) and (f), it can be inferred that the mockup had an ultimate strength higher than 650 kN,
 681 which deteriorated to around 600 kN at the end of the PsD test. Besides, as shown in Figure 21(f), the mockup started to

682 exhibit a negative stiffness and also a drop of strength at about 2.1% top storey drift. Degradation of stiffness was also
 683 observed, as also demonstrated in Figure 22, which shows the initial stiffness at the beginning of each test. The lateral
 684 stiffness was initially around 90 kN/mm but dropped to about 60 kN/mm after ‘Test 3’ due to cracks on the infill. The
 685 large reduction of stiffness was noticed at the start of the third ground motion of ‘Test 4’, during which the stiffness
 686 decreased from 60 to 30 kN/mm as cracks on the infill became more severe. Eventually, the lateral stiffness dropped to
 687 around 15 kN/mm during ‘Test 5’, during which the damage on the infill walls became more extensive due to the increased
 688 ground motions intensity.
 689
 690
 691

Table 22. Comparison of peak base shear obtained numerically and experimentally (unit: kN).

	Test 3	Test 4			Test 5	
	GM1	GM1	GM2	GM3	GM1	GM2
Test mockup	542	403	660	296	662	619
Liberatore-Decanini	311	246	328	152	356	365
Fardis-Panagiotakos	703	115	160	77	235	314

692



(e) (f)
 Figure 21. Cyclic response of the mockup: (a) Test 3; (b) Test 4-GM1; (c) Test 4-GM2; (d) Test 4-GM3; (e) Test 5-GM1; (f) Test 5-GM2.

693
 694
 695
 696
 697
 698
 699
 700
 701
 702
 703
 704
 705
 706
 707
 708
 709
 710
 711
 712
 713
 714
 715
 716

By comparing the numerical results with the experimental measurements, it can be seen in Figure 21(f) that the Liberatore-Decanini model had an ultimate strength of around 350 kN, which was 46% lower than the real strength of the test frame. Nevertheless, it only showed negative stiffness during the second ground motion of ‘Test 5’, which agrees with the experimental observations. On the other hand, the Fardis-Panagiotakos model showed an ultimate strength of about 700 kN, which was slightly higher than the test frame’s real capacity, as can be seen in Figure 21(a). However, its masonry infill on the ground failed during the first test by reaching the residual strength, which explained the considerably lower strength of this model in the following tests (*i.e.*, less than 200 kN during ‘Test 4’ and around 300 kN during ‘Test 5’). The Fardis-Panagiotakos model reached its ultimate strength at about 0.07% top storey drift, which was very small compared to the 2.1% drift of the test frame and the 0.78% drift of the Liberatore-Decanini model. This result was consistent with the measured initial stiffness and fundamental period (see Figure 15 and Table 20). Apart from that, the total failure of masonry struts in the Fardis-Panagiotakos model during ‘Test 3’ suggested that it had a very steep post-peak negative stiffness, which led to the quick loss of strength of the infills at very small displacements. It can then be concluded that the Liberatore-Decanini model significantly underestimated the strength of test frame, so that the relevant formulae to determine the strength associated with different damage patterns need further investigation since the interaction between the local struts and the column flanges is not accounted for. Meanwhile, although the Fardis-Panagiotakos model provided a ‘good’ estimate of ultimate strength, it does not achieve the same level of accuracy for other experimental tests, as formerly pointed out by Mohammad Noh *et al.* [21]. Moreover, due to the much higher initial stiffness, as shown in Figure 22, both models underestimated the displacement considerably at both ultimate strength and the onset of residual strength, since those displacements depend on the initial stiffness. Lastly, as demonstrated in Figure 22, the stiffness of the mockup was found to be considerably overestimated by the selected modelling strategies before the PsD test. However, as the damage on the infill wall became more severe, the stiffness of the numerical models became closer to the actual stiffness of the mockup.

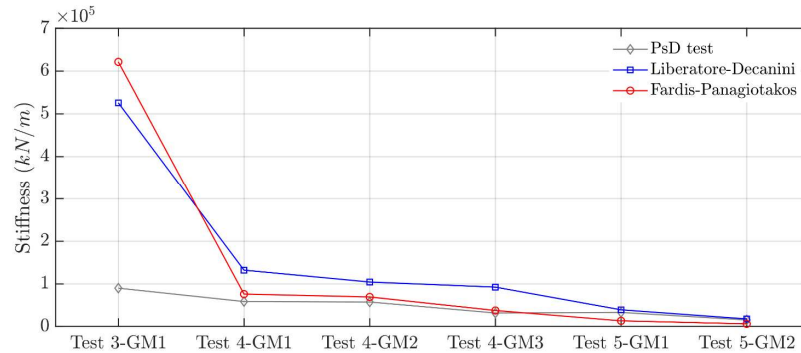
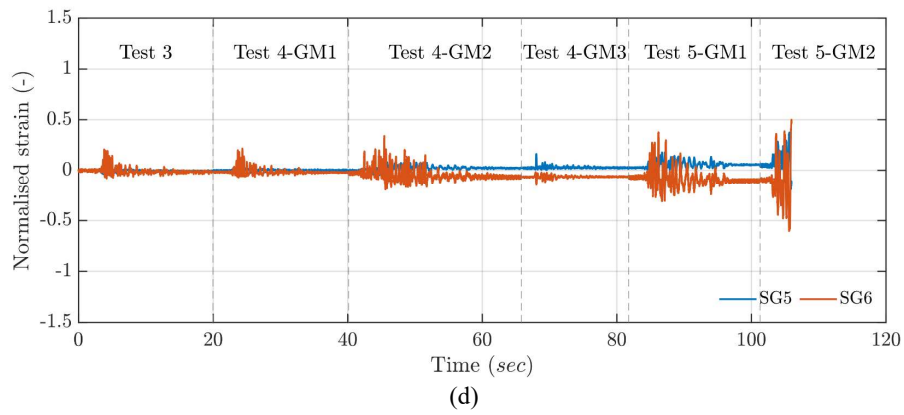
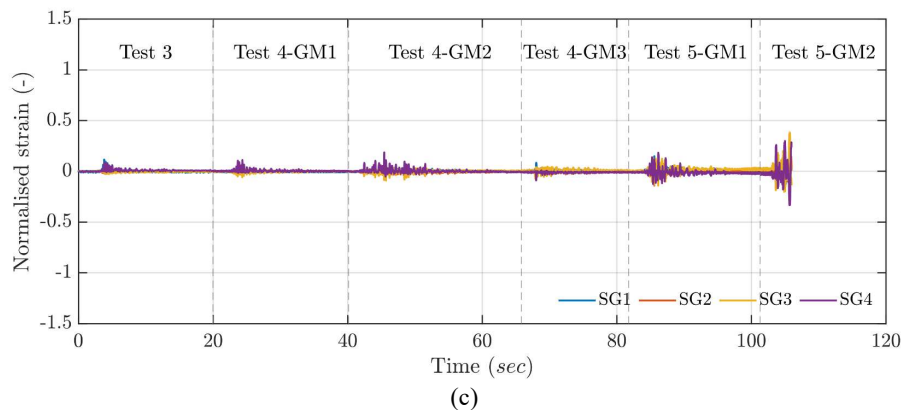
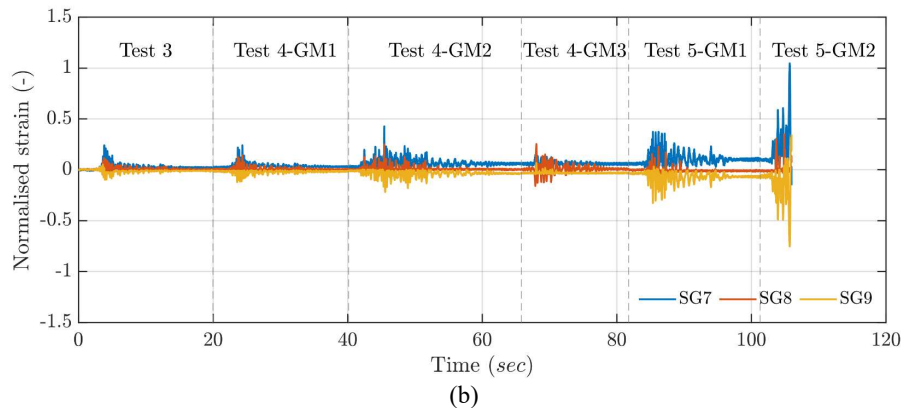
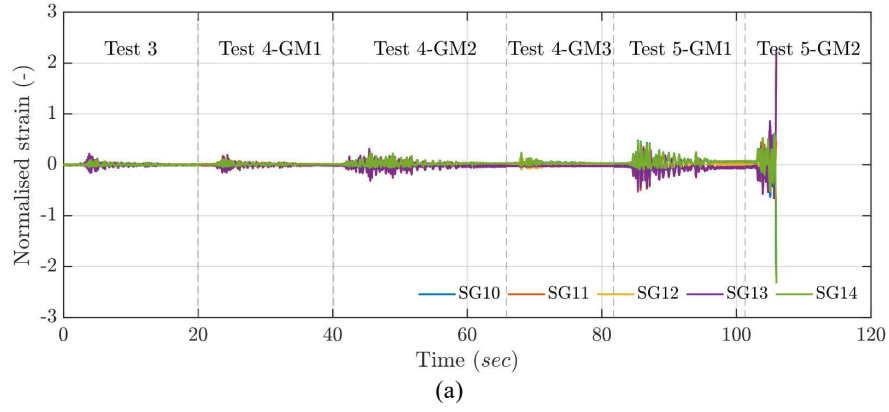


Figure 22. Comparison of the initial stiffness of the mockup at the beginning of each test.

717
 718
 719
 720
 721
 722
 723
 724
 725
 726
 727
 728
 729
 730
 731
 732
 733
 734
 735
 736

Figure 23 presents the strain measured at certain cross-sections of steel components of the test mockup (See Figure 12(b) for the locations of monitored cross-sections and the strain gauges), which are normalised to the strain at yielding obtained from the coupon test. It can be seen that no yielding was detected until the last cycle of the PsD test, where yielding was noticed in the first floor column only, as shown in Figure 23(a) and (b). For the p column where yielding was detected, yielding only occurred in its flanges while its web remained elastic. Besides, large plastic deformation was found at the cross-section close to the column base, with a peak strain of more than twice the yield strain, as shown in Figure 23(a). On the other hand, the top region of the first floor column was anticipated to experience limited plastic deformation, as shown in Figure 23(b), since the peak strain at the monitored cross-section only slightly exceeds the yield strain. Lastly, the monitored cross-sections of the first floor beam remained elastic throughout the entire PsD test, which suggested that all beams of the test mockup were not damaged.

During the PsD test, a few cycles of free vibration were added to the end of each ground motion in order to identify the period elongation and investigate the impact of the earthquake sequence. The obtained periods are summarised in Table 23. It can be seen that the mockup experienced a significant reduction of stiffness after ‘Test 3’, which is ascribable to the cracks of masonry infills. The mockup’s measured period after ‘Test 3’ was about three times longer than the initial period. For the rest of the PsD test, slight period elongation was also identified but to a much less extent, despite more extensive damages on the masonry infills.



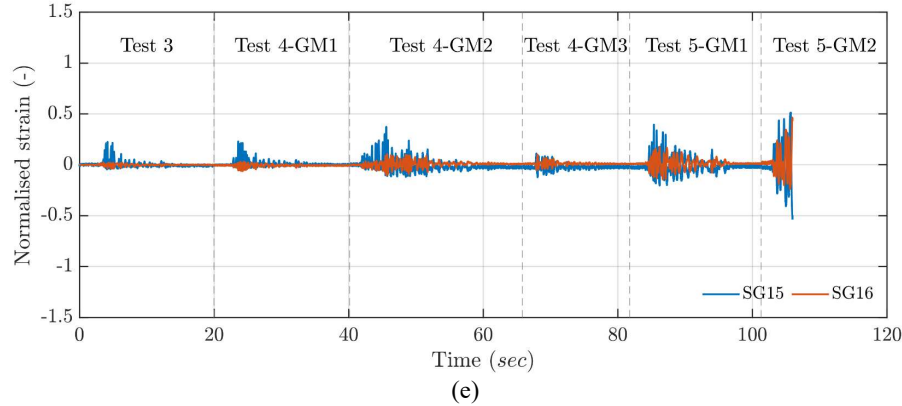


Figure 23. Normalised strain (unit strain at yielding) measured at signeted cross-sections of column and beam (See Figure 12(b)): (a) Detail 1; (b) Detail 2; (c) Detail 3; (d) Detail 4; (e) Detail 5.

Table 23. Period of the mockup after each test (unit: sec).

Initial	Test 3	Test 4			Test 5
	GM1	GM1	GM2	GM3	GM1
0.142	0.429	0.444	0.455	0.455	0.474

6 CONCLUSIONS

This paper investigates the influence of masonry infills on the seismic response under earthquake sequences of a steel moment-resisting frame representative of existing European buildings non-conforming to modern seismic codes. The steel frame was assessed in two configurations; the prototype building was a two-storey three-bay moment frame, while the experimental mockup was composed by the central bay sub-structure of the 75% scaled prototype building. The research activity was carried out in two phases that are addressed in two parts of this paper.

In the first part, the seismic performance of the prototype building is evaluated by means of non-linear static analyses and the limitations of the current EC8-3 for dealing with the presence of masonry infills are also identified. The main conclusions are summarised as follows:

- Modelling only the bare frame may significantly overestimate the seismic demands of steel MRFs, since the increased stiffness and strength due to masonry infill is neglected.
- The presence of masonry infills may also increase the severity of soft-storey mechanism. Numerical models showed that the presence of masonry infills reduced the displacement capacities of about 40% compared to the capacities of the bare frame in case of soft-storey mechanism;
- The N2 method currently recommended by the EC8-3 for representing the seismic demands is unable to handle the typical pushover curves of infilled structures, as it assumes bi-linearisation of pushover curves. N2 method for infilled structures should be included in the next generation of EC8-3, along with appropriate safety criteria for determining the capacities of masonry infills.

In the second part, the results of experimental tests on the mockup were presented and compared with existing modelling strategies of masonry infill in literature. The experimental outcomes allowed to draw the following remarks:

- The damage observed on the infill walls comprised, in the order of occurrence, a local damage mode, *i.e.* cracks at top corners of infills, and three global damage modes, including diagonal tension (cracking), sliding shear and diagonal compression mode;
- The local crush and cracks at top corners of infill walls were due to the interlock between bolts in the beam splice connections and the top layer of brick, which caused the formation of local struts at top corners of infill walls and might have effectively prevented the corner crush damage mode due to the formation of global diagonal struts across the infill wall panels. This is considered a distinctive feature of the infilled steel frame from RC frame;
- The flanges of the steel column may be able to provide some constraints on the out-of-plane deformation of the infill wall, thus delaying the occurrence of diagonal compression damage mode (out-of-plane failure). The effects of column flanges should be further investigated both numerically and experimentally;

- 775 • The cyclic response of the infilled frame showed significant pinching effects, which was due to the opening and
776 closing of cracks in the infilled walls. The pinching effects were more severe during ground motions with higher
777 intensities;
- 778 • Uniformly distributed infill wall may also trigger soft storey mechanism, especially when most of the infill walls
779 on the same floor are about to lose their load carrying capacity;
- 780 • Experimental results showed that the mockup's fundamental period became nearly three times longer during the
781 first PsD test after the cracks at the top corners of the infill wall. However, during the rest of PsD test, the periods
782 elongation was considered minor, indicating that the degradation of stiffness during the earthquake sequence
783 was not significant;
- 784 • The Liberatore-Decanini model underestimated the ultimate strength of the test frame by around 46%, while the
785 Fardis-Panagiotakos model slightly overestimated the ultimate strength by less than 10%;
- 786 • Both the Liberatore-Decanini model and Fardis-Panagiotakos model significantly overestimated the initial
787 stiffness of the mockup by about three times. This overestimation of initial stiffness also affected other
788 parameters defining the backbone curves, thus leading to smaller displacement at both the ultimate strength and
789 the onset of residual strength.

790 ACKNOWLEDGEMENTS

791 The financial support of the Seismic Engineering Research Infrastructure (SERA) project (European Commission,
792 H2020-INFRAIA-2016-2017, Agreement No.730900) to HITFRAMES project is greatly acknowledged. Any opinions,
793 findings and conclusions, or recommendations expressed in this paper are those of the Authors and do not necessarily
794 reflect those of SERA Sponsors.
795

796 REFERENCES

- 797 1. Federal Emergency Management Agency (FEMA). State of the art report on past performance of steel moment-frame
798 buildings in earthquakes, 2000, Washington, DC.
- 800 2. Di Sarno L, Paolacci F, Sextos AG. Seismic Performance Assessment of Existing Steel Buildings: A Case Study,
801 *Key Engineering Materials* 2018; 763:1067-1076.
- 802 3. Clifton C, Bruneau M, MacRae G, Leon R, Fussell A. Steel structures damage from the Christchurch earthquake
803 series of 2010 and 2011. *Bulletin of the New Zealand Society for Earthquake Engineering* 2011; 44(4):297-318.
- 804 4. Mahin SA. Lessons from damage to steel buildings during the Northridge earthquake. *Engineering structures* 1998;
805 20(4-6):261-270.
- 806 5. Tremblay R, Filiatrault A, Timler P, Bruneau M. Performance of steel structures during the 1994 Northridge
807 earthquake. *Canadian Journal of Civil Engineering* 1995; 22(2):338-360.
- 808 6. Okazaki T, Lignos DG, Midorikawa M, Ricles JM, Love J. Damage to steel buildings observed after the 2011
809 Tohoku-Oki earthquake. *Earthquake spectra* 2013; 29(1_suppl):219-243.
- 810 7. Miranda E, Mosqueda G, Retamales R, Pekcan G. Performance of non-structural components during the 27 February
811 2010 Chile earthquake. *Earthquake Spectra* 2012; 28(1_suppl1):453-471.
- 812 8. Saatcioglu M, Tremblay R, Mitchell D, Ghobarah A, Palermo D, Simpson R, Adebar P, Ventura C, Hong H.
813 Performance of steel buildings and non-structural elements during the 27 February 2010 Maule (Chile) Earthquake.
814 *Canadian Journal of Civil Engineering* 2013; 40(8):722-734.
- 815 9. European Committee for Standardization (CEN). Eurocode 8: Design of structures for earthquake resistance - Part 3:
816 Assessment and retrofitting of buildings, 2005, Brussels, Belgium.
- 817 10. Gutiérrez-Urzúa F, Freddi F, Di Sarno L. Comparative analysis of code-based approaches for seismic assessment of
818 existing steel moment resisting frames. *Journal of Constructional Steel Research* 2021; 181:106589.
- 819 11. Fardis MN, Panagiotakos TB. Seismic design and response of bare and masonry-infilled reinforced concrete
820 buildings part II: infilled structures. *Journal of Earthquake Engineering* 1997; 1(03):475-503.
- 821 12. Dolšek M, Fajfar P. The effect of masonry infills on the seismic response of a four-storey reinforced concrete frame-
822 a deterministic assessment. *Engineering Structures* 2008; 30(7):1991-2001.
- 823 13. El-Dakhkhni WW, Elgaaly M, Hamid AA. Three-strut model for concrete masonry-infilled steel frames. *Journal of*
824 *Structural Engineering* 2003; 129(2):177-185.
- 825 14. Dawe JL, Seah CK. Behaviour of masonry infilled steel frames. *Canadian Journal of Civil Engineering* 1989;
826 16(6):865-876.
- 827 15. Markulak D, Radić I, Sigmund V. Cyclic testing of single bay steel frames with various types of masonry infill.
828 *Engineering structures* 2013; 51:267-277.
- 829 16. Di Sarno L, Wu JR. Seismic assessment of existing steel frames with masonry infills. *Journal of Constructional Steel*
830 *Research* 2020; 169:106040.

- 833 17. Decanini, LD, Fantin G. Modelos simplificados de la mampostería incluidas en porticos. Características de resistencia
834 en el estado límite, VI Jornadas Argentinas de Ingeniería Estructural, 1986, Buenos Aires, Argentina.
- 835 18. Crisafulli FJ, Carr AJ. Proposed Macro-Model for the Analysis of Infilled Frame Structures. *Bulletin of the New*
836 *Zealand Society for Earthquake Engineering* 2007; 40(2):69–77.
- 837 19. Liberatore L, Decanini LD. Effect of infills on the seismic response of high-rise RC buildings designed as bare
838 according to Eurocode 8. *Ingegneria sismica* 2011; 3:7-23.
- 839 20. Uva G, Raffaele D, Porco F, Fiore A. On the role of equivalent strut models in the seismic assessment of infilled RC
840 buildings, *Engineering Structures* 2012; 42:83-94.
- 841 21. Mohammad Noh N, Liberatore L, Mollaioli F, Tesfamariam S. Modelling of masonry infilled RC frames subjected
842 to cyclic loads: State of the art review and modelling with OpenSees. *Engineering Structures* 2017; 150:599-621.
- 843 22. Liberatore L, Noto F, Mollaioli F, Franchin P. In-plane response of masonry infill walls: Comprehensive
844 experimentally-based equivalent strut model for deterministic and probabilistic analysis, *Engineering Structures*
845 2018; 167:533-548.
- 846 23. Di Sarno L. Effects of multiple earthquakes on inelastic structural response. *Engineering Structures* 2013; 56:673-
847 681.
- 848 24. Hatzigeorgious G, Beskos D. Inelastic displacement ratios for SDOF structures subjected to repeated earthquakes.
849 *Engineering Structures* 2009; 31(11):2744-2755.
- 850 25. Jalayer F., Ebrahimian H. Seismic risk assessment considering cumulative damage due to aftershocks. *Earthquake*
851 *Engineering and Structural Dynamics* 2017; 46(3):369-389.
- 852 26. Li Q, Ellingwood B. Performance evaluation and damage assessment of steel frame buildings under main shock-
853 aftershock earthquake sequences. *Earthquake Engineering and Structural Dynamics* 2007; 36(3):405-427.
- 854 27. Ruiz-Garcia J, Negrete-Manriquez JC. Evaluation of drift demands in existing steel frames under as-recorded far-
855 field and near-fault mainshock-aftershock seismic sequences. *Engineering Structures* 2011; 33:621-634.
- 856 28. Li Y, Song R, Van De Lindt JW. Collapse fragility of steel structures subjected to earthquake mainshock-aftershock
857 sequences. *Journal of Structural Engineering* 2014; 140(12):04014095.
- 858 29. Ruiz-García J, Aguilar JD. Aftershock seismic assessment taking into account post-mainshock residual drifts.
859 *Earthquake Engineering and Structural Dynamics* 2015; 44(9):1391-1407.
- 860 30. Tesfamariam S, Goda K, Mondal G. Seismic vulnerability of reinforced concrete frame with unreinforced masonry
861 infill due to mainshock-aftershock earthquake sequences. *Earthquake Spectra* 2015; 31(3):1427-1449.
- 862 31. Burton HV, Sharma M. Quantifying the reduction in collapse safety of mainshock-damaged reinforced concrete
863 frames with infills. *Earthquake Spectra* 2017; 33(1): 25-44.
- 864 32. Furtado A, Rodrigues H, Varum H, Arêde A. Mainshock-aftershock damage assessment of infilled RC structures.
865 *Engineering Structures* 2018; 175:645-660.
- 866 33. Di Trapani F, Malavisi M. Seismic fragility assessment of infilled frames subject to mainshock/aftershock sequences
867 using a double incremental dynamic analysis approach. *Bulletin of Earthquake Engineering* 2019; 17:211-235.
- 868 34. Aljawhari K, Freddi F, Galasso C, Gentile R. Effects of ground-motion sequences on fragility and vulnerability of
869 case-study reinforced concrete frames. *Bulletin of Earthquake Engineering* 2020; 3:1-31.
- 870 35. Ricles JM, Lignos DG, Love J, Midorikawa M, Okazaki T. Tohoku Japan Earthquake and Tsunami Clearinghouse.
871 2012 [cited 2020 July 14]. In: Learning From Earthquakes [Internet]. Available from:
872 <http://learningfromearthquakes.org/2011-03-11-tohoku-japan/>
- 873 36. Takanashi K, Udagawa K, Seki M, Okada T, Tanaka H. Nonlinear earthquake response analysis of structures by a
874 computer-actuator on-line system. *Bulletin of Earthquake Resistant Structure Research Center* 1975; 8:1-7.
- 875 37. Pegon P, Pinto AV. Pseudo-dynamic testing with substructuring at the ELSA Laboratory. *Earthquake Engineering*
876 *and Structural Dynamics* 2000; 29(7):905-925.
- 877 38. Shing PB, Mahin SA. Pseudodynamic method for seismic performance testing: theory and implementation. 1984,
878 Earthquake Engineering Research Center, University of California, Berkeley.
- 879 39. Nakashima M, Kato H, Takaoka E. Development of real-time pseudo dynamic testing. *Earthquake Engineering and*
880 *Structural Dynamics* 1992; 21(1):79-92.
- 881 40. Nakashima M. Development, potential, and limitations of real-time online (pseudo-dynamic) testing. *Philosophical*
882 *Transactions of the Royal Society of London. Series A: Mathematical, Physical and Engineering Sciences* 2001;
883 359(1786):1851-1867.
- 884 41. Sadeghian V, Kwon OS. Discussion of “Fast and Slow Cyclic Tests for Reinforced Concrete Columns with an
885 Improved Axial Force Control” by Yunbyeong Chae, Jinhaeng Lee, Minseok Park, and Chul-Young Kim. *Journal*
886 *of Structural Engineering* 2020; 146(7):07020001.
- 887 42. Mojiri S, Kwon OS, Christopoulos C. Development of a ten-element hybrid simulation platform and an adjustable
888 yielding brace for performance evaluation of multi-story braced frames subjected to earthquakes. *Earthquake.*
889 *Engineering and Structural Dynamics.* 2019; 48(7):749-771.
- 890 43. McKenna F, Scott MH, Fenves GL. Non-linear finite-element analysis software architecture using object
891 composition. *Journal of Computing in Civil Engineering* 2010; 24:95-107.

- 892 44. European Committee for Standardization (CEN). Eurocode 8: Design of structures for earthquake resistance - Part 1:
893 General rules, seismic actions and rules for buildings, 2004, Brussels, Belgium.
- 894 45. Krawinkler H, Seneviratna GD. Pros and cons of a pushover analysis of seismic performance evaluation. *Engineering*
895 *Structures* 1998; 20(4-6):452-464.
- 896 46. Fajfar P, Gašperšič P. The N2 method for the seismic damage analysis of RC buildings. *Earthquake Engineering and*
897 *Structural Dynamics* 1996; 25(1):31-46.
- 898 47. European Committee for Standardization (CEN). Eurocode 3: Design of steel structures - Part 1-1: General rules and
899 rules for buildings, 2011, Brussels, Belgium.
- 900 48. Freddi F, Dimopoulos CA, Karavasilis TL. Experimental evaluation of a rocking damage-free steel column base with
901 friction devices. *Journal of Structural Engineering* 2020; 146(10):04020217.
- 902 49. British Standards Institution (BSI), BS EN ISO 6892-1: Metallic materials-Tensile testing-Part 1: Method of test at
903 room temperature, 2020, London, UK.
- 904 50. British Standard Institution (BSI). BS EN 1052-1:1999, Methods of test for masonry. Determination of compressive
905 strength, 1999, London, UK.
- 906 51. European Committee for Standardization (CEN). Eurocode 6: Design of masonry structures. General rules for
907 reinforced and unreinforced masonry structures, 2005, Brussels, Belgium.
- 908 52. ASTM International, ASTM E519 Standard test method for diagonal tension (shear) in masonry assemblages, 2015,
909 West Conshohocken, PA.
- 910 53. Lignos DG, Krawinkler H. Deterioration modelling of steel components in support of collapse prediction of steel
911 moment frames under earthquake loading. *Journal of Structural Engineering* 2011; 137(11):1291-1302.
- 912 54. Zareian F, Medina RA. A practical method for proper modelling of structural damping in inelastic plane structural
913 systems. *Computers and Structures* 2010; 88(1-2):45-53.
- 914 55. Luzi L, Puglia R, Russo E, ORFEUS WG. Engineering Strong Motion Database, version 1.0. *Istituto Nazionale di*
915 *Geofisica e Vulcanologia, Observatories & Research Facilities for European Seismology*, 2016.
- 916 56. American Society of Civil Engineering (ASCE). ASCE41-17: Seismic Evaluation and Retrofit of Existing Buildings,
917 2007, Reston, Virginia.
- 918 57. Dolšek M, Fajfar P. Simplified non-linear seismic analysis of infilled reinforced concrete. *Earthquake Engineering*
919 *and Structural Dynamics* 2004; 34(1):49-66.
- 920 58. Asteris PG, Antoniou ST, Sophianopoulos DS, Chrysostomou CZ. Mathematical macromodeling of infilled frames:
921 state of the art. *Journal of Structural Engineering* 2011; 137(12):1508-1517.